![Argonne National Laboratory logo]

Characterization of Intergranular Fission Gas Bubbles in U-MO Fuel

Nuclear Engineering Division

Characterization of Intergranular Fission Gas Bubbles in U-MO Fuel

by
Y.S. Kim, G.L. Hofman, and J. Rest
Nuclear Engineering Division, Argonne National Laboratory

February 14, 2008

Table of Contents

List of Figures

List of Tables

Summary

This report can be divided into two parts: the first part, which is composed of sections 1, 2, and 3, is devoted to report the analyses of fission gas bubbles; the second part, which is in section 4, is allocated to describe the mechanistic model development.

Swelling data of irradiated U-Mo alloy typically show that the kinetics of fission gas bubbles is composed of two different rates: lower initially and higher later. The transition corresponds to a burnup of ~40 at% U-235 (LEU) or a fission density of ~3×10^{21} fissions/cm^3. Scanning electron microscopy (SEM) shows that gas bubbles appear only on the grain boundaries in the pre-transition regime. At intermediate burnup where the transition begins, gas bubbles are observed to spread into the intragranular regions. At high burnup, they are uniformly distributed throughout fuel.

In highly irradiated U-Mo alloy fuel large-scale gas bubbles form on some fuel particle peripheries. In some cases, these bubbles appear to be interconnected and occupy the interface region between fuel and the aluminum matrix for dispersion fuel, and fuel and cladding for monolithic fuel, respectively. This is a potential performance limit for U-Mo alloy fuel.

Microscopic characterization of the evolution of fission gas bubbles is necessary to understand the underlying phenomena of the macroscopic behavior of fission gas swelling that can lead to a counter measure to potential performance limt. The microscopic characterization data, particularly in the pre-transition regime, can also be used in developing a mechanistic model that predicts fission gas bubble behavior as a function of burnup and helps identify critical physical properties for the future tests.

Analyses of grain and grain boundary morphology were performed. Optical micrographs and scanning electron micrographs of irradiated fuel from RERTR-1, 2, 3 and 5 tests were used. Micrographic comparisons between as-fabricated and as-irradiated fuel revealed that the site of first bubble appearance is the grain boundary. Analysis using a simple diffusion model showed that, although the difference in the Mo-content between the grain boundary and grain interior region decreased with burnup, a complete convergence in the Mo-content was not reached at the end of the test for all RERTR tests.

A total of 13 plates from RERTR-1, 2, 3 and 5 tests with different as-fabrication conditions and irradiation conditions were included for gas bubble analyses. Among them, two plates contained powders γ-annealed at ~800°C for ~100 hours. Most of the plates were fabricated with as-atomized powders except for two as-machined powder plates. The Mo contents were 6, 7 and 10wt%. The irradiation temperature was in the range 70 – 190°C and the fission rate was in the range 2.4×10^{14} – 7×10^{14} f/cm^3-s.

Bubble size for both of the γ-annealed powder plates is smaller than the as-atomized powder plates. The bubble size for the as-atomized powder plates increases as a function of burnup and the bubble growth rate shows signs of slowing at burnups higher than ~40 at% U-235 (LEU). The bubble-size distribution for all plates is a quasi-normal, with the average bubble size ranging

0.14 - 0.18 µm. Although there are considerable errors, after an initial incubation period the average bubble size increases with fission density and shows saturation at high fission density.

Bubble population (density) per unit grain boundary length was measured. The γ-annealed powder plates have a higher bubble density per unit grain boundary length than the as-atomized powder plates. The measured bubble number densities per unit grain boundary length for as-atomized powder plates are approximately constant with respect to burnup.

Bubble density per unit cross section area was calculated using the density per unit grain boundary length data. The grains were modeled as tetrakaidecahedrons. Direct measurements for some plates were also performed and compared with the calculated quantities.

Bubble density per unit grain boundary surface area was calculated by using the density per unit grain boundary length data. These data were used as input for mechanistic modeling described in section 4.

Volumetric bubble density was calculated by using density per unit grain boundary surface area. Based on these data, bubble volumetric fraction was calculated. Bubble volume fraction was also calculated by using the density per unit cross section area. Bubble volume fraction was also directly measured for some plates. These three results are comparable although the direct measurement data are slightly larger than the others. Bubble volume fraction increased as a function of burnup, reaching ~2% of fuel volume at $3x10^{21}$ f/cm^3. Fission gas bubble swelling is minor compared to that of solid fission product swelling. This suggests that in the pre-transition regime a considerable concentration of fission gas remains in atomic solution or in small bubbles not resolvable by SEM.

The mechanistic model presented here considers analytical solutions to coupled rate equations that describe the nucleation and growth of inter- and intragranular bubbles under the simultaneous effect of irradiation-induced gas-atom re-solution. The goal of the formulation is to avoid a coupled set of nonlinear equations that can only be solved numerically, using instead a simplified, physically reasonable hypothesis that makes the analytical solutions viable. The gas-induced swelling rate is then assessed by calculating the evolution of the bubble population with burn-up and subsequently the amounts of gas in bubbles and lattice sites. Uncertain physical parameters of the model are adjusted by fitting the calculated bubble populations at given burn-ups with measured bubble size and density data.

Calculations of intergranular bubble size distribution made with this new mechanistic model of grain boundary bubble formation kinetics is consistent with the measured distributions. The gas-atom diffusion enhancement factor for grain boundaries was determined to be $7x10^3$ in order to obtain agreement with the measured distributions. This value of enhancement factor is consistent with values obtained in the literature. The enhancement factor is about six times higher for as-fabricated powder plates than for the annealed plates, due to the lower Mo content on the boundaries. Model predictions are sensitive to various model parameters such gas-atom diffusivity and re-solution rate. Improved prediction capability requires an accurate quantification of these critical materials properties and measurement data.

1. Introduction

Addition of 2 wt% or more of silicon to the Al matrix has been demonstrated to be effective in reducing interaction layer (IL) growth in U-Mo/Al dispersion fuel irradiated in the RERTR-6 (~40 at% U-235) test and the RERTR-7A (~100 at% U-235 LEU equiv.) test (see Fig. 1). At high burnup, however, large fission gas pores formed within fuel particles. In some cases, the connection between pores on fuel peripheries appears to have separated the fuel from the matrix. Because the volume expansion due to IL growth in the Si-modified matrix plates is negligible, large fission gas pore formation within the fuel is a potential life-limiting factor at very high burnup such as achieved in the RERTR-7A test.

Three types of bubbles are observed in high burnup U-Mo fuel. The first type is found in the interior part of a fuel particle (A in Fig.1). These bubbles are small in size, and evenly distributed throughout the fuel. These are denoted bulk bubbles. The second type of bubble is larger in size than the bulk bubbles and forms at the contact plane of two neighboring fuel particles (B in Fig.1). These are termed intersection bubbles. The third type of bubble is located at the fuel particle periphery (C in Fig.1). These bubbles are relatively large and unevenly distributed. At high burnup, these bubbles tend to coalesce to form large-scale pores. It appears that there are threshold burnups for the formation of the second and third type bubble.

In spite of the difference in type, the initial stage of bubble formation is considered similar for all bubbles. Therefore, characterization of bulk bubbles at the initial stage (burnup less than ~40 at% U-235) is considered critical for developing a mechanistic model which includes a capability to assess where and how various type bubbles grow.

Post irradiation U-Mo fuel cross sections show the characteristic bulk bubble morphology for several burnup levels, as shown in Fig. 2. Fission gas bubbles first appear on linear features, heterogeneously over the fuel cross section (shown in (a)). The linear features are likely grain boundaries. There are virtually no bubbles observed in the interior of the grains. As burnup increases (~40-50 %U-235), the bubble population increases on the grain boundaries and additional bubbles progressively spread to the interior regions (shown in (b)). At this stage, the fuel swelling rate increases. The phenomenon underlying this increase in bubble nucleation and growth is grain refinement or 'recrystallization' of the γ U-Mo. Eventually at higher burnup, bubbles uniformly cover the entire fuel cross section (shown in (c)).

Developing a mechanistic fuel swelling model is important to assess fuel performance and to assist in interpretation of post irradiation examination (PIE) results. In particular, characterization of bubbles at the initial stage (burnup less than ~40 at% U-235) is considered critical for developing a mechanistic model which includes a capability to assess where and how the bubbles grow as a function of burnup. This is a first step towards the identification of the factor or the combination of factors that leads to the pore growth at the fuel periphery.

The work presented in this report is thus limited to fission gas bubble formation and fuel swelling mechanisms to burnups up to ~40 at%U-235 or fission density of $3x10^{21}$ f/cm^3. The study at higher burnups involves more complicated phenomena and will be the subject of a future report.
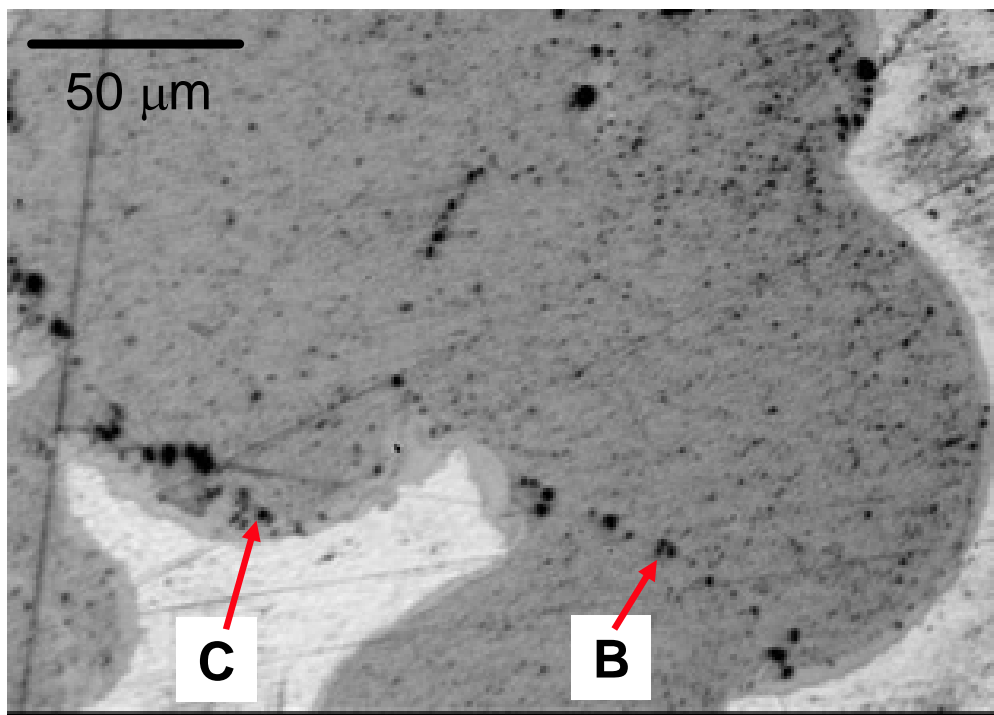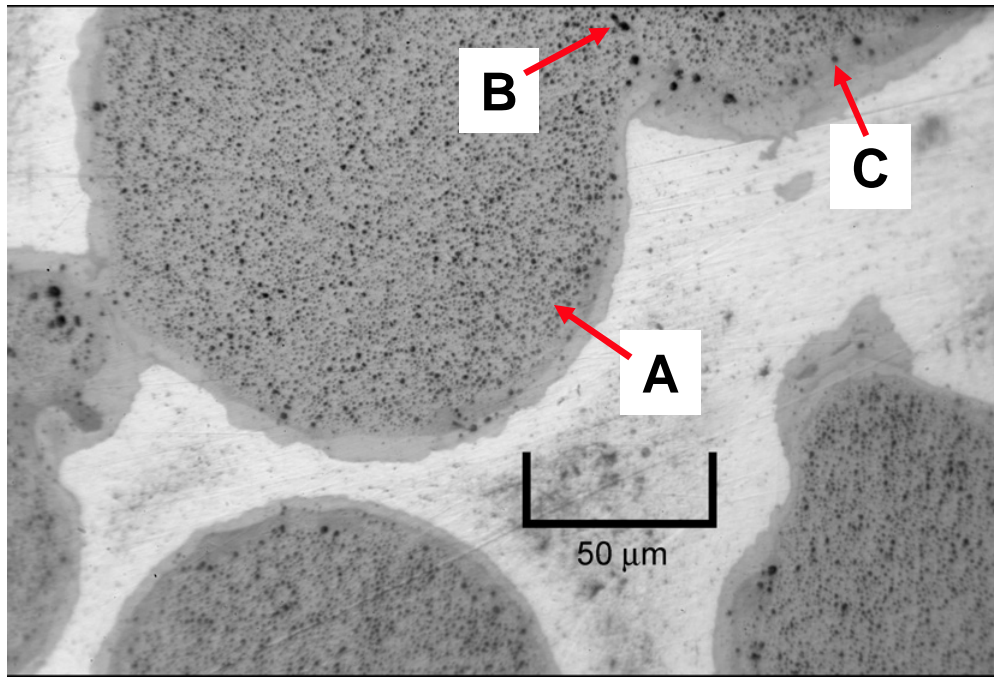
Fig. 1 OM (optical microscopy) photos showing microstructure of hot side of R2R040 from RERTR-7A. Burnup of this region is 90 at%U-235 (LEU equiv.). The gray areas are fuel and bright areas are Al matrix. The black spots in fuel are fission gas bubbles. The interaction layers located along the intersection of the fuel particles and the aluminum matrix are very thin.
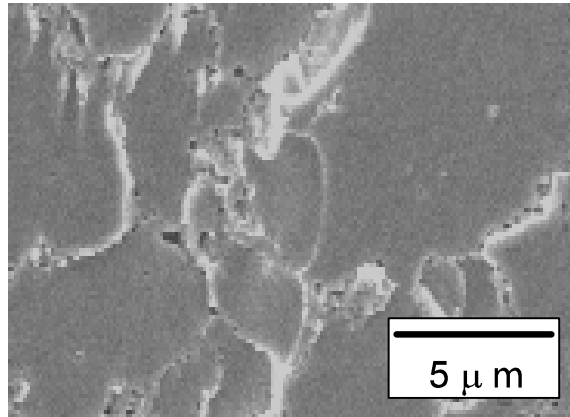
(a) 35 %U-235 BU (V6018G from RERTR-5)
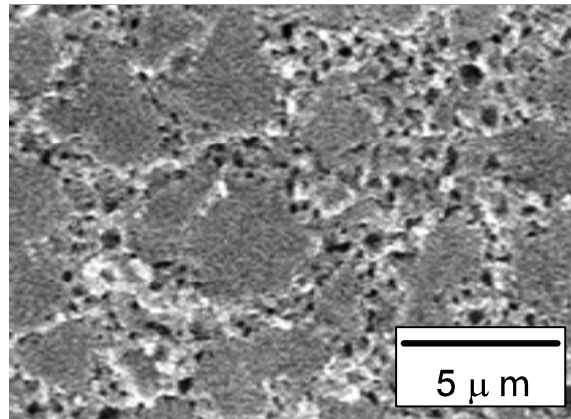
(b) 65 %U-235 BU (V6001M from RERTR-4)
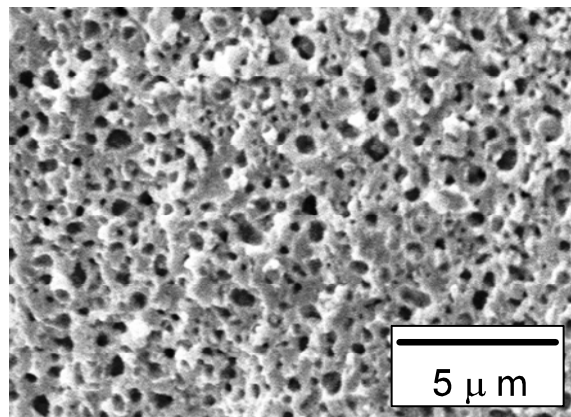
(c) 80 %U-235 BU (V6022M from RERTR-4)

Fig. 2 SEM (scanning electron microscopy) photos of irradiated U-Mo fuels from
RERTR-4 and 5. The samples shown in this figure were fabricated with the
same batch of atomized fuel particles and irradiated at similar temperatures.

3

2. Characterization of grain and grain boundary

Two kinds of fuel particles were used in the miniplate tests, viz., centrifugally atomized particles and machined chips made from homogenized cast alloy rods.

2.1 Pre-irradiation grain morphology of atomized U-Mo

The microstructure of the atomized powder consists of a "cellular" solidification structure which is commonly found in rapidly cooled alloys that have a pronounced solidus-liquidus gap. When the U-10Mo melt (or $U_{0.78}Mo_{0.22}$) in the U-Mo phase diagram shown in Fig. 3 is cooled, the melt follows the right arrow (line A). When it meets the liquidus line, $U_{0.64}Mo_{0.36}$ solidifies as solid islands. As the cooling progresses, the solid phase volume increases and simultaneously the Mo content in the solid phase decreases. In the atomization process, however, the cooling does not follow this equilibrium process. Instead, once it meets the solidus line, the remaining liquid phase, which consists of a lower Mo-content than the solid islands, solidifies abruptly leaving an interconnected network with a lower Mo-content. The boundaries between the cells most likely form low angle grain boundaries.

The region, when etched, may appear as a thick boundary because of its low Mo-content and obscures the thinner grain boundaries. We can consider this as effective grain boundaries. In this report we call these simply 'grain boundaries.'

Because the swelling rate of U-Mo alloy increases as the Mo content decreases, it is arguable that the lower Mo-content region near the grain boundaries has a more favorable environment for bubble nucleation.

A similar process for a lower Mo-content alloy, such as U-7Mo, is shown by the left arrow (B in Fig. 3). The gap between the solidus and liquidus lines on arrow B is slightly smaller than on arrow A. Thus, U-7Mo will have slightly smaller solid islands, i.e., smaller grains than U-10Mo. In addition, the grain boundary Mo content of U-7Mo is lower than that of U-10Mo.

The average cell size, i.e., in our terminology 'grain size,' reported by Kim et al [1] is ~2 μm for an atomized U-10Mo powder. Our measurement using an SEM picture of an as-fabricated RERTR-3 plate from the memo by Sinkler et al. [2] yielded a grain size of 2.5 μm surrounded by grain boundaries that lie within a ~0.5-μm thick zone of a nominally lower Mo concentration.

Atomized U-Mo fuel particles typically consist of colonies of the aforementioned small grains (cells) often of columnar shape enclosed by what appear to be primary γ grain boundaries. In Fig. 4, the grain structure is shown for an extra-ordinarily large particle (~200 μm) recently fabricated in KAERI [3]. The thicker boundaries are primary grain boundaries grouping colonies of smaller grains. This sample should have similar general characteristics as U-Mo alloy despite the addition of 1 wt% Zr. Because of its larger-than-standard size, the grain size is probably larger than that of the standard size fuel particle used in RERTR tests (~75 μm). The grain size in this sample particle is in the range of 2 - 12 μm.
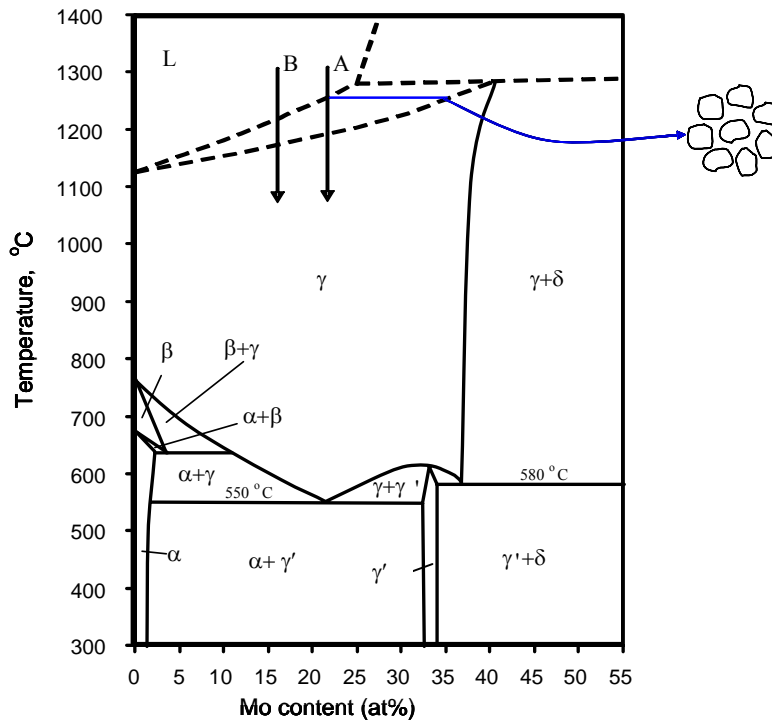
Fig. 3 U-Mo phase diagram.
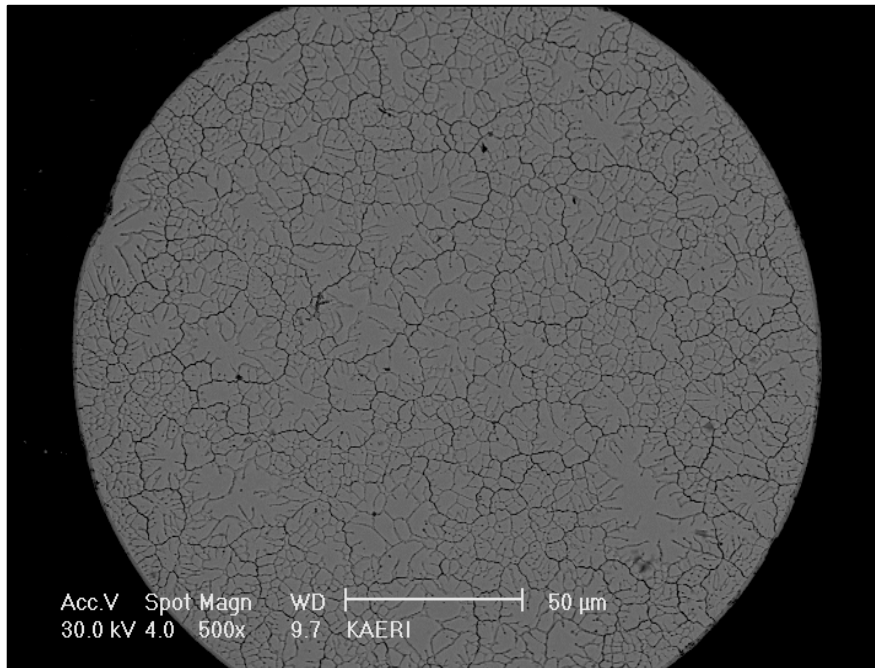
Fig. 4 SEM image of a U-7Mo-1Zr alloy particle after metallographic etching [2]. This fuel particle is larger (~200 μm) than the typical size (~75 μm) used in RERTR-3 plates.

2.2 Homogenization of 'cored' microstructure during irradiation

In order to assess what extent the as-solidified 'cored' Mo concentration will be eliminated as a result of fission enhanced diffusion, we use Bleiberg's analysis of α+γ' to γ phase reversal during fissioning. Bleiberg [4,5] reported that the α phase lamellae initially spaced by the thin γ' phase layers in U-Mo alloy fuel disappeared during irradiation to a burnup of ~0.1 at% total U burnup (LEU equiv. 0.5%U-235 burnup). The average distance between the α lamellae centers was 0.5 μm and their thickness was 0.2 μm. Bleiberg concluded that phase homogenization was sensitive to the fission rate and the distance between lamella centers.

We derived a model to analyze grain homogenization time, schematically shown in Fig. 5, in an analogous manner to the Bleiberg model. We assumed Bleiberg's model is also applicable to our single-phase case because the Mo concentration difference at the grain boundary and the grain interior region is substantial. The as-fabricated Mo concentration at the grain interior is estimated to be 22 at% and that at the grain boundary 17 at% [1,2].

(a) Schematic of a grain boundary in slab geometry, and Mo concentration

(b) Schematic of Mo concentration difference between grain boundary and grain interior
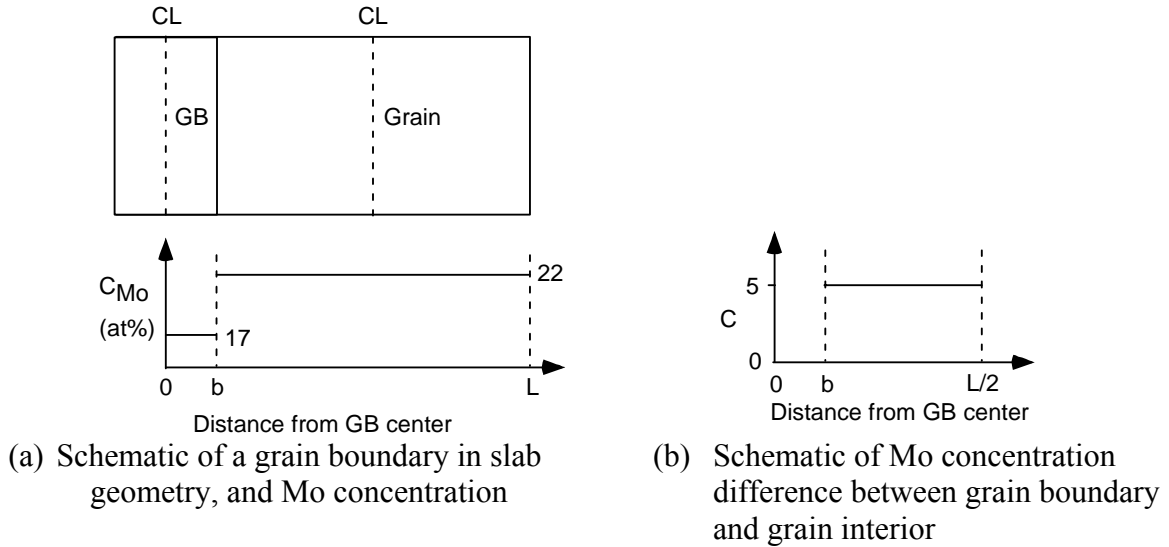
Fig. 5 Model of the initial condition of grain and grain boundary and corresponding Mo-concentration. CL=centerline, GB=grain boundary, b=half of GB thickness, L=distance between two neighbor grain centers (i.e., grain size).

For simplicity, we assume the diffusion coefficient of Mo is constant with respect to Mo concentration and dependent only on the fission rate, given by $D = \frac{1}{12} f_r V^{5/3}$ where f_r is the fission rate and V is the volume affected by a fission spike (2.01×10^{-18} cm^3), and we also assume the fission rate is constant throughout irradiation. Then, the diffusion process is governed by Fick's equation:

$$\frac{\partial C(x,t)}{\partial t} = D \frac{\partial^2 C(x,t)}{\partial x^2} \qquad (1)$$

with the boundary and initial conditions,

$$\frac{\partial C}{\partial x} = 0 \qquad at \ x = 0, \ L/2,$$

$$C(x,0) = 0 \qquad 0 \le x \le b; \quad C(x,0) = 5 \qquad b \le x \le L/2 \tag{2}$$

The solution is similar to that obtained by Bleiberg [4] as follows:

$$C(x,t) = \frac{2}{L} \int_0^{L/2} C(x,0)dx + \frac{4}{L} \sum_{n=1}^{\infty} \int_0^{L/2} C(x,0)cos\left(2n\pi\frac{x}{L}\right)dx \ cos\left(2n\pi\frac{x}{L}\right)exp\left(-4Dn^2\pi^2\frac{t}{L^2}\right) \tag{3}$$

Expanding the series in Eq.(3) to $n=10$, we obtained the change in Mo concentration as a function of time at the grain boundary and grain interior as shown in Fig. 6.

As seen in Fig. 6, the Mo concentration at the grain center and the grain boundary converge with time. Complete homogenization, however, takes ~2000 days. For the RERTR-3 plates, the concentration difference between the grain center and the grain boundary is still 2.5 at% at EOL (or 48 EFPD). For this analysis, we used grain size=3 μm and grain-boundary 'width'=0.5 μm (see section 2.1 and Table 1).
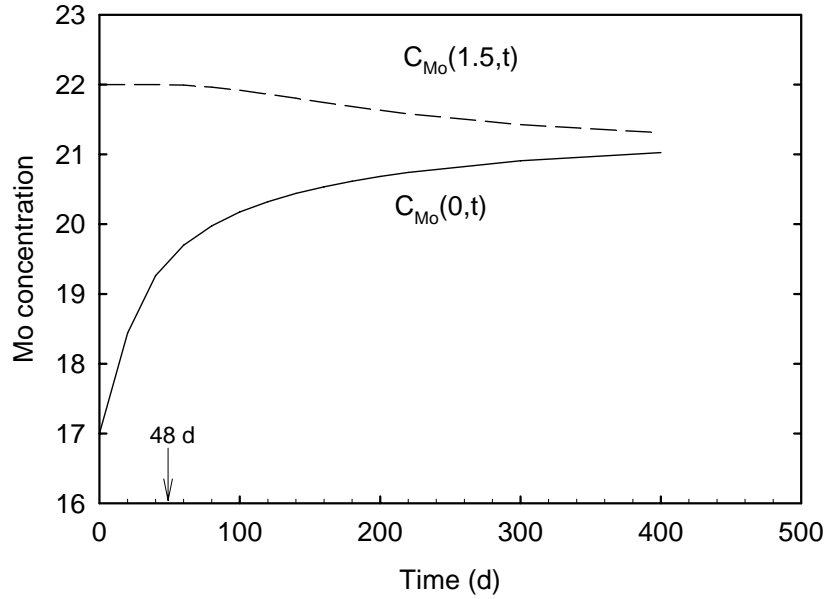
Fig. 6 Time-dependent Mo concentration. $C_{Mo}(1.5,t)$ is the time-dependent Mo concentration at the grain center, $C(0,t)$ is the time-dependent Mo concentration at the grain boundary center. Data used for the calculation are: fission rate=6×10^{14} f/cm³-s, D=1.6×10^{-16} cm²/s, grain size (L)=3 μm, grain boundary width (2b)=0.5 μm.

From this analysis, we conclude that, for the given irradiation condition of typical RERTR-3 plates, the grain boundaries remain at a lower Mo-concentration until EOL.

2.3 Pre-irradiated microstructure of machined U-Mo

Machined powders are heavily cold worked and contain a high concentration of dislocations. During hot rolling of the fuel plates and subsequent irradiation this dislocation structure will undergo polygonization. Apparently the final subgrain structure of machined powders is similar to that of the atomized ones, providing nucleation sites for gas bubbles. Machined powders are made from well homogenized cast alloy rods, and therefore do not contain the 'cored' cellular structure typical of the rapidly solidified atomized powders.

In addition to as-fabricated fuel powders, two powders one from atomized and the other from machined powders, were annealed before plate fabrication in the γ-phase to obtain powders with a homogeneous γ microstructure. Thus, both coring and cold working effects were removed. Fig. 7 shows examples of both types of annealed fuel powders. The microstructures are rather similar consisting of relatively large grains determined (by X-ray diffraction) as cubic γ U-Mo [3].

(a) Machined powder (Y02) (b) Atomized powder (Z02)
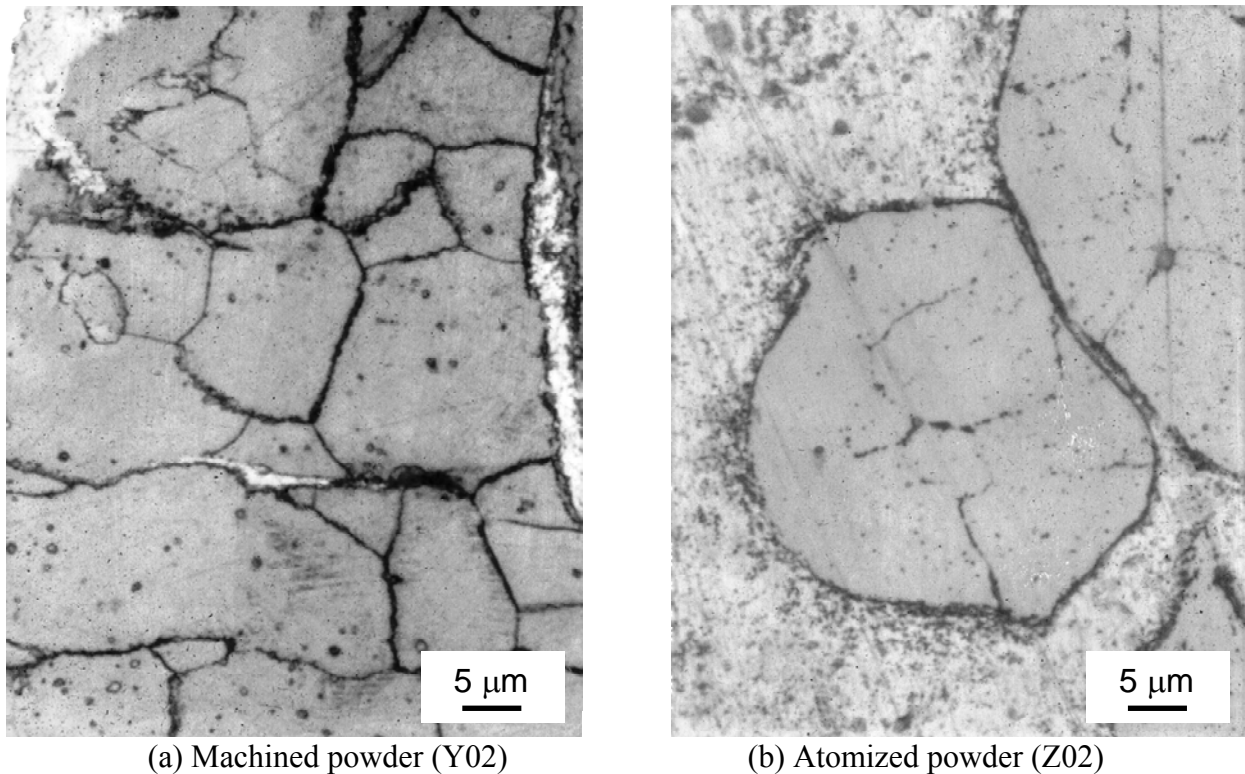
Fig. 7 OM micrographs of γ-annealed powder plates. Y02 and Z02 are the siblings of Y01 and Z03, respectively.

2.4 Post irradiation measurement of grain size

To determine the average grain size, we selected three plates from irradiated RERTR-3 plates for the measurement. They are Z03, V03, and S03. The description of the plates is given in Table 1. These plates included atomized powders supplied by KAERI. Z03 contains a γ phase annealed powder. Annealing was performed for 100 hours at 800°C. The grains grew considerably and only large grains are present in the fuel particles. Z03 and V03 contain U-10Mo whereas S03 has U-6Mo. As-fabricated U-Mo powders were used in V03 and S03. The grain morphology is considered to be the same for these plates as discussed earlier in Sect. 2.1. These two plates are considered typical plates in the RERTR-3 test.

Z03 and Y01

As a result of γ-annealing, there are only large grains in Z03 and Y01 as shown in Figs. 8 and 9, respectively. These figures show that the cellular or subgrain structure has been eliminated.
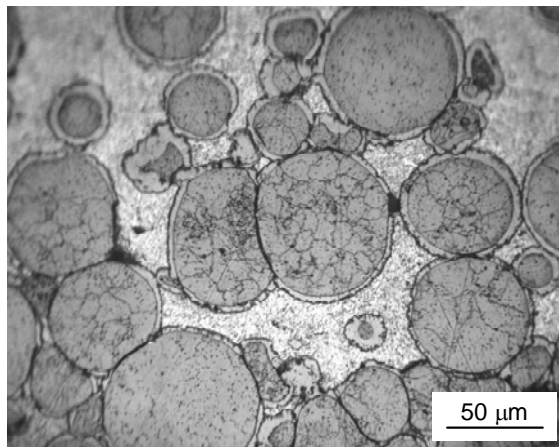
(a) Optical microscopy of Z03.
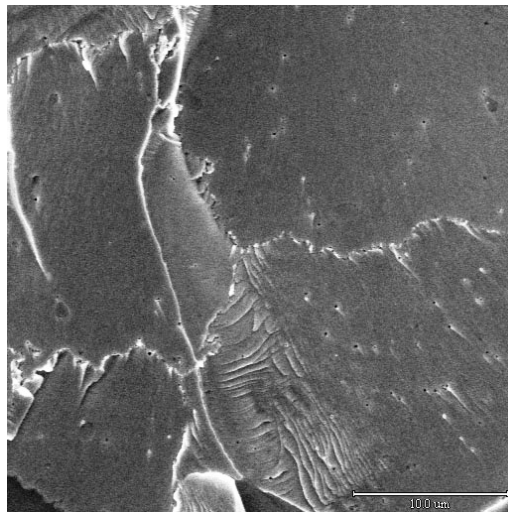
(b) SEM of Z03. The scale bar is for 10 μm

Fig. 8 OM and SEM micrographs of Z03. Z03 fuel powder was γ-phase annealed for 100 hours at 800°C before plate-fabrication.
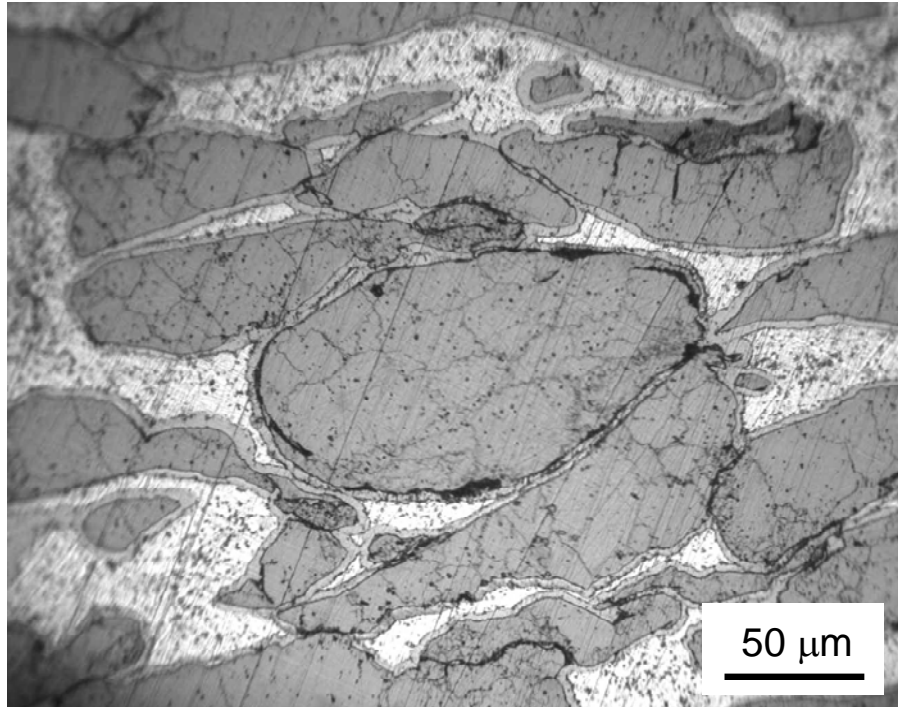
(a) Optical microscopy of Y01.
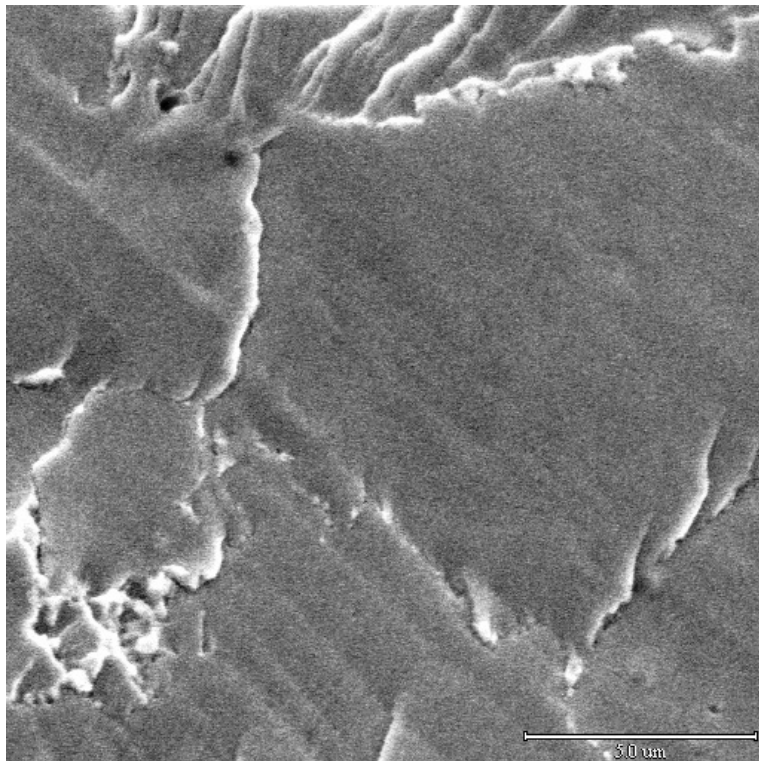
(b) SEM of Y01. The scale bar is for 5 μm.

Fig. 9 OM and SEM micrographs of Y01. Y01 fuel powder was γ-phase annealed for 100 hours at 800°C before plate-fabrication.

The bubble morphology observed in the SEM photos of Figs. 8 and 9 is different from other as-atomized plates such as V03 and S03. The bubbles in Z03 and Y01 are smaller in size as well as fewer in number than the other plates. This is attributed to differences in the condition in the fuel.

Although bubbles are not visible in the OM photo, comparison between the OM photo and SEM photo shows that the lines along which bubbles are observed on the OM photo match the grain boundaries in the SEM photo.

For the machined chips in Y01, the subgrain boundaries have largely disappeared and grain growth has occurred during the 800°C anneal for 70 hours.

V03

The size and shape of the grains vary within the particles; smaller at the periphery than in the interior part, and frequently columnar in shape in the periphery whereas equiaxed in the interior. The grain size measurement from the SEM picture in Fig. 10 (b) is consistent with the measurement for grains from the as-fabricated plate as discussed in Section 3. As discussed for Z03, bubbles are not visible in the OM photo. Comparison between the OM photo and SEM photo shows that the lines in the OM photo are grain boundaries in the SEM photo.

The grain size distribution measured on the OM photo of Fig. 10 (a) for V03 is given in Fig. 11. Although there are some large grains observed, the predominant size is about 4 μm for this fuel.
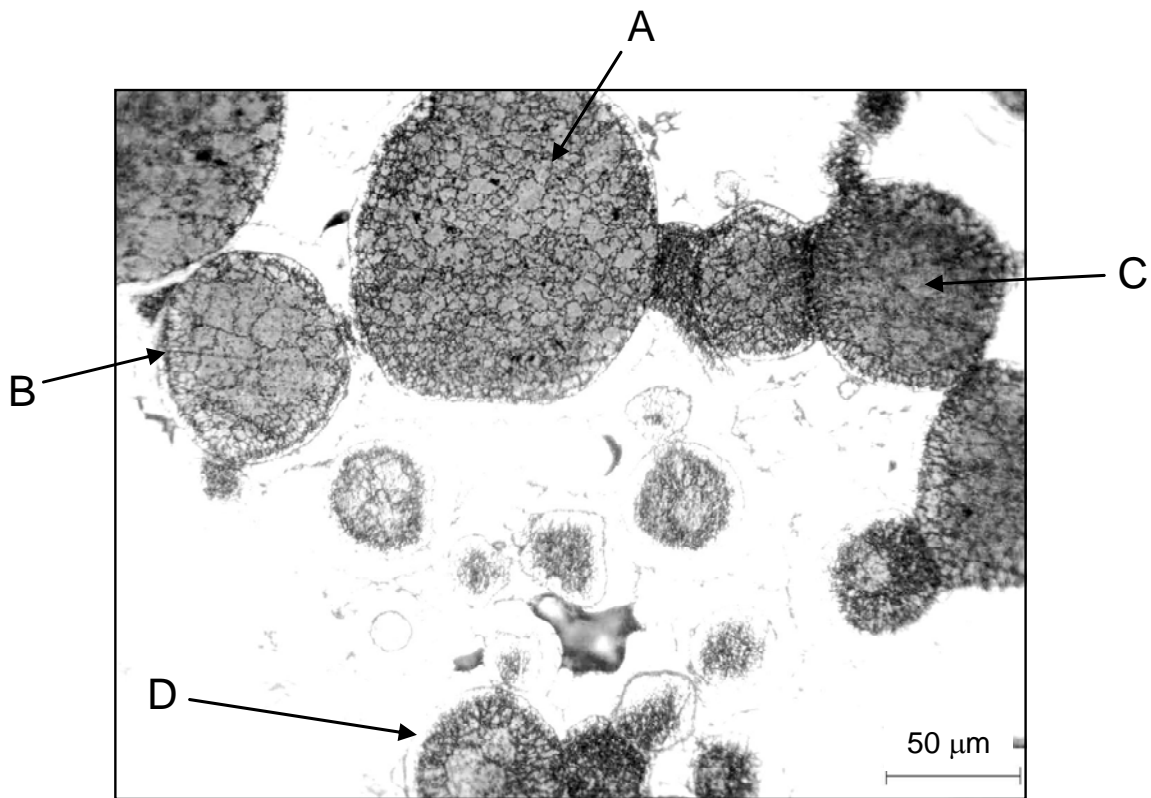
Fig. 10 (a) OM of V03.
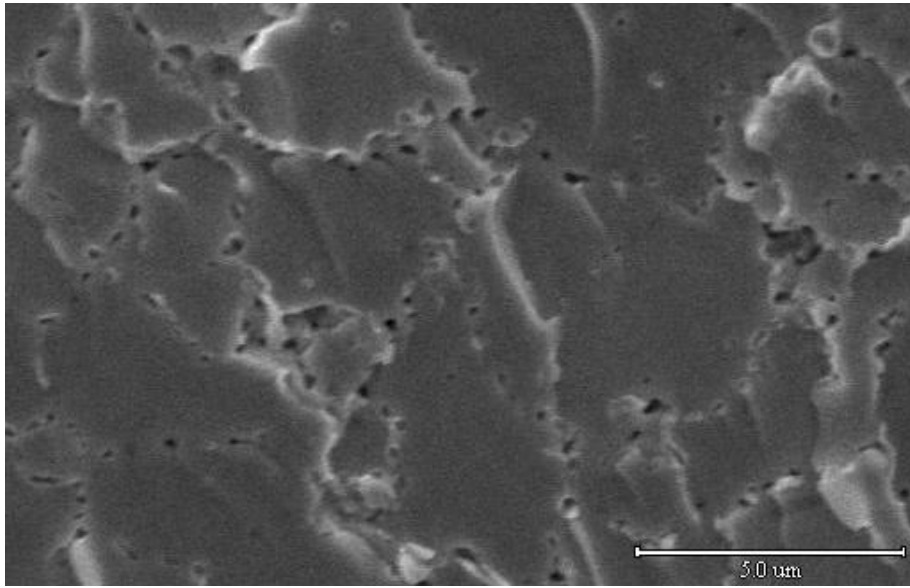
Fig. 10 (b) SEM of V03.

RERTR-3 580W
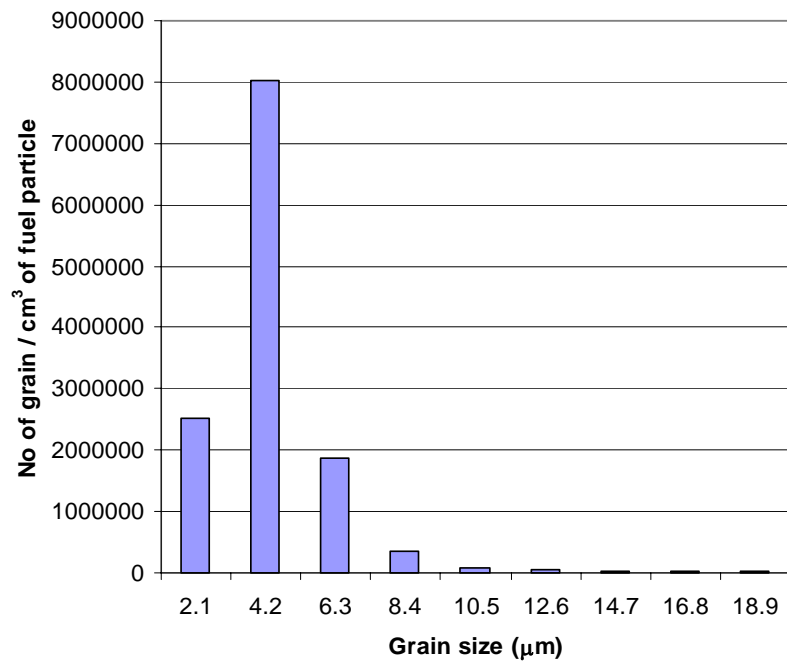
Fig. 11 Grain size distribution in V03.

S03

The same analysis as for V03 was performed. An optical micrograph is shown in Fig. 12. The grain and bubble morphology of S03 (U-6Mo fuel) is similar to that of V03. This is additional confirmation that bubble formation first happens on the grain boundaries. The formation of bubbles invisible with SEM, i.e., smaller than the SEM resolution ~0.02 μm, most likely takes place within intragranular regions. However, the relatively large bubbles visible in SEM are only found on the grain boundaries. A recent Belgian TEM study of irradiated U-Mo fuel showed that intragranular bubbles of ~0.002 μm indeed form homogeneously throughout the fuel matrix [6].
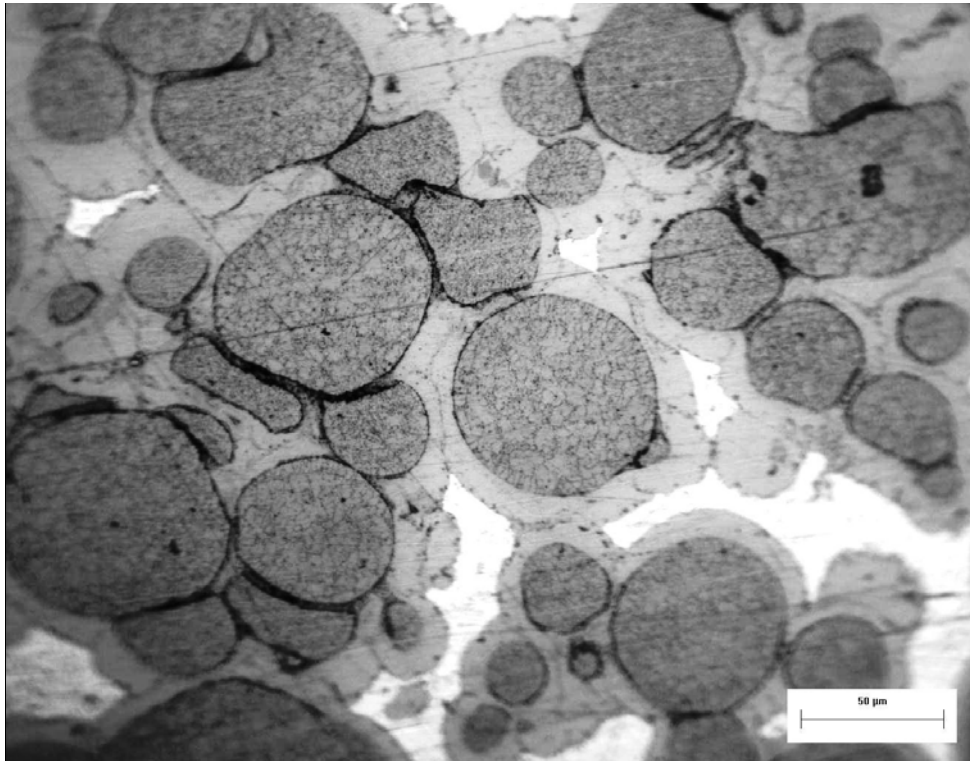
Fig. 12 OM of S03.

From the OM and SEM observations of Z03, V03 and S03, we can conclude that the observed bubbles with SEM are intergranular.

In table 1, the measured grain sizes are given. The lineal intercept method [7] was used and checked with the Saltykov method [7]. The lineal intercept method uses several straight lines in different directions on a cross section of a fuel particle, and the number of intersections with grain boundaries is counted. The grain size is the average of the values obtained by dividing line length with the number of intersections for each line.

Table 1. Grain size measurement for RERTR-3 plates

Fuel	Z03	V03	S03
	Atomized U-10Mo	Atomized U-10Mo	Atomized U-6Mo
	γ- annealed	as-fabricated	as-fabricated
Size and method	32.4%U-235 BU	37.6%U-235 BU	38.6%U-235 BU
OM photo (μm)	16	4	4
SEM photo (μm)	19	3	3

3. Quantitative analysis of intergranular bubbles

3.1 Bubble size and population distribution on grain boundaries

In Table 2 the irradiation conditions for the fuel plates used in the analysis are summarized [8].

Table 2. Description of fuel used in the analysis

Test	Plate AG ID	Plate ID	Fuel property	Burn up, at% U-235	Fission rate (10^{14}) f/cm^3-s	Total duration (days)	Fuel Temp (^{o}C)
RERTR-3	580H	Z03	U-10Mo(a,γ)	32	5.3	48	121
RERTR-3	580C	Y01	U-10Mo(m,γ)	30	4.8	48	109
RERTR-1	H-3 *	V002	U-10Mo(a)	39	3.8	94	66
RERTR-1	H-4 *	A003	U-10Mo(m)	40	3.8	94	68
RERTR-3	580G	V07	U-10Mo(a)	30	5.1	48	122
RERTR-3	580W	V03	U-10Mo(a)	38	6.3	48	149
RERTR-3	580Z	S03	U-6Mo(a)	39	7.0	48	158
RERTR-5	600Y	A6008H	U-10Mo(a)	49	3.1	116	177
RERTR-5	600AG	R6007F	U-7Mo(a)	37	2.4	116	185
RERTR-5	600M	V6019G	U-10Mo(a)	49	2.9	116	142
RERTR-5	600D	V6018G	U-10Mo(a)	35	2.3	116	121
RERTR-5	600AH	V8005B	U-10Mo(a)	37	2.4	116	170
RERTR-5	600V	A8002L	U-10Mo(m)	48	2.9	116	191

a: atomized, m: machined, γ: annealed at 800°C for 70 -100 hours.
*: capsule position

Figures 13-25 present the measured bubble size distributions. This information was used for the calculation of the average bubble diameter shown in Table 3.

All the results provided here are based on the measurements from SEM images of fracture surfaces. Because the fracture surfaces are not perfectly flat, bubble-containing features are not perfect lineal intercepts with the underlying grain boundaries. Also readings on SEM pictures with lower magnifications lead to uncertainties in the measurements. These experimental limitations may explain some of the variability in the measured bubble size distributions. For some plates, different SEM pictures were available to obtain better counting statistics. The uncertainties related to the bubble size measurements are $\pm 10\%$, which leads to uncertainties $\pm 20\%$ in the spans between the maximum and minimum bubble sizes. The bubble size populations for the middle bins are less affected by these uncertainties than those towards both ends. The errors for the middle bins are $\pm 10\%$ and for the end bins $\pm 50\%$.

The bubble size and number are measured on bubble-containing boundaries. For each SEM picture, the maximum and minimum bubble sizes were measured. The difference between the maximum and minimum was divided by seven. Therefore, for each fuel plate, seven size groups are used to characterize the bubble distribution.
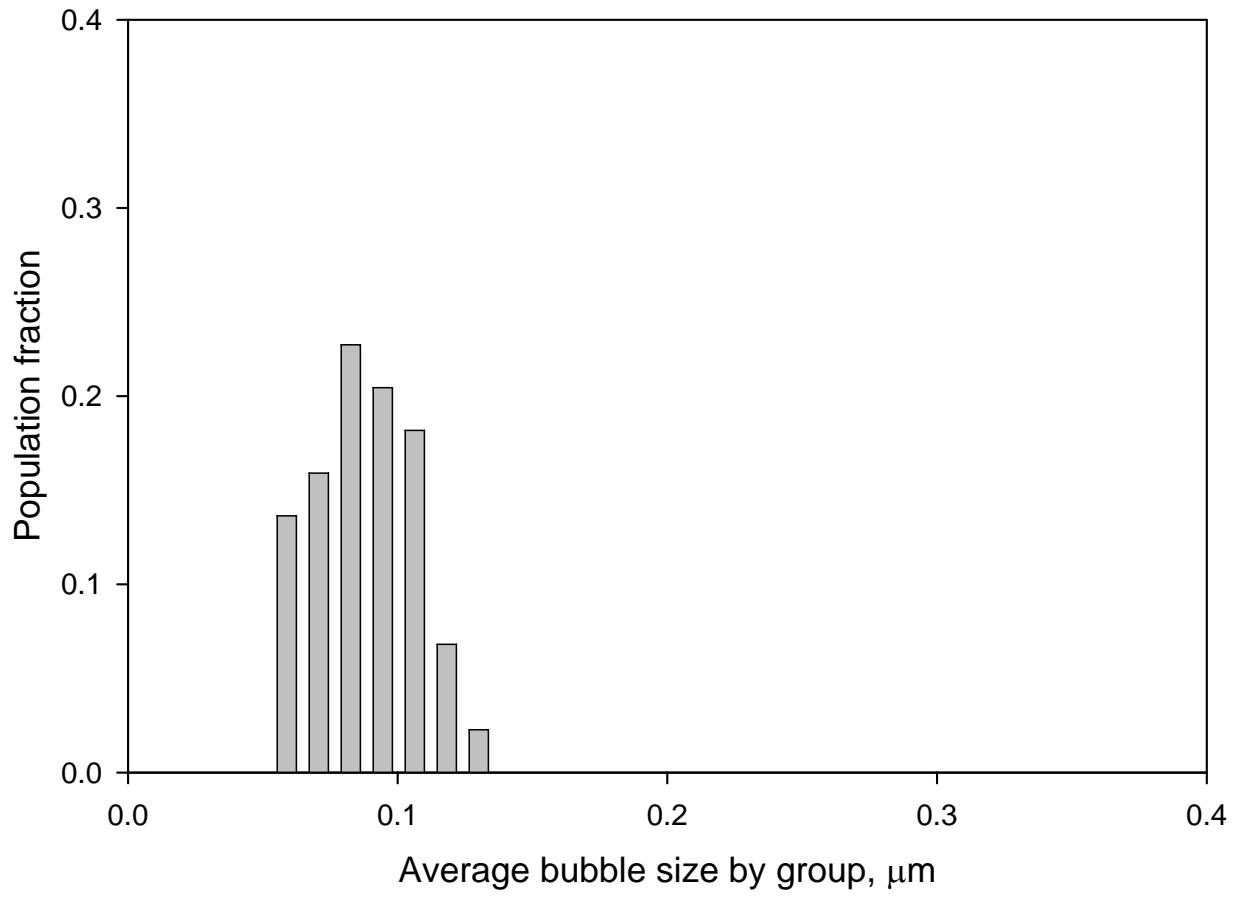
Fig. 13 Bubble size distributions for 580H-Z03 plate from RERTR-3 (γ-annealed).
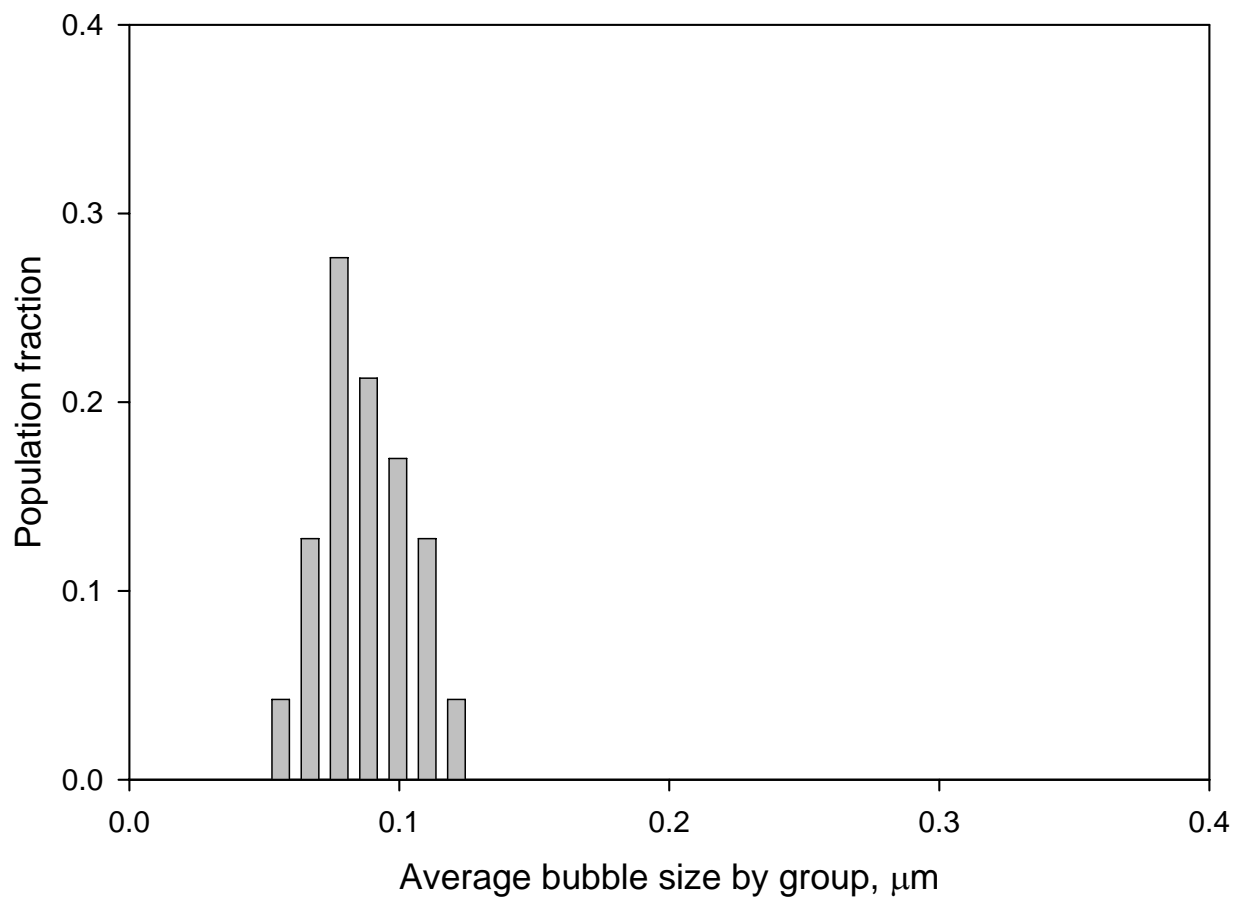
Fig. 14 Bubble size distribution for 580C-Y01 plate from RERTR-3 (γ-annealed).
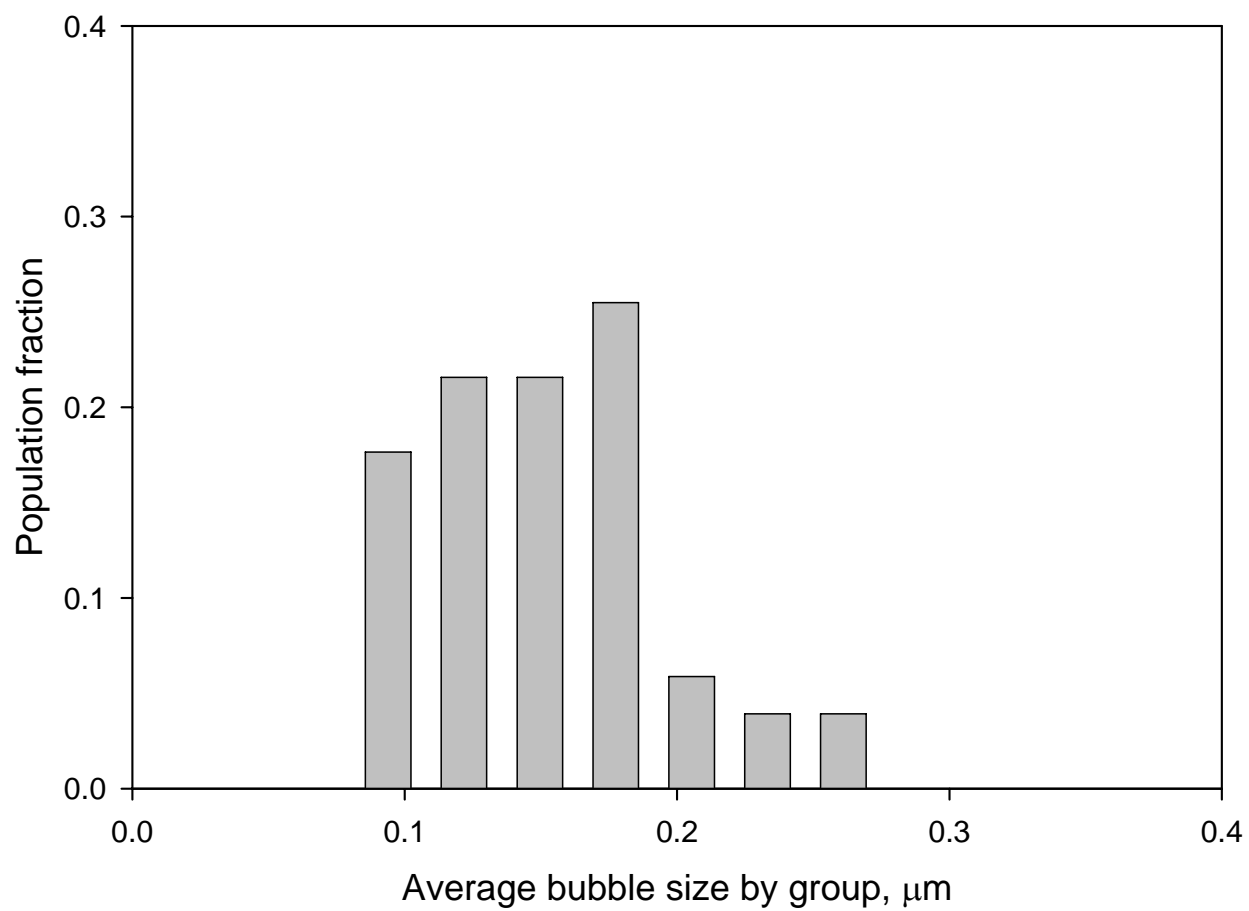
Fig. 15 Bubble size distribution for V002 plate from RERTR-1.
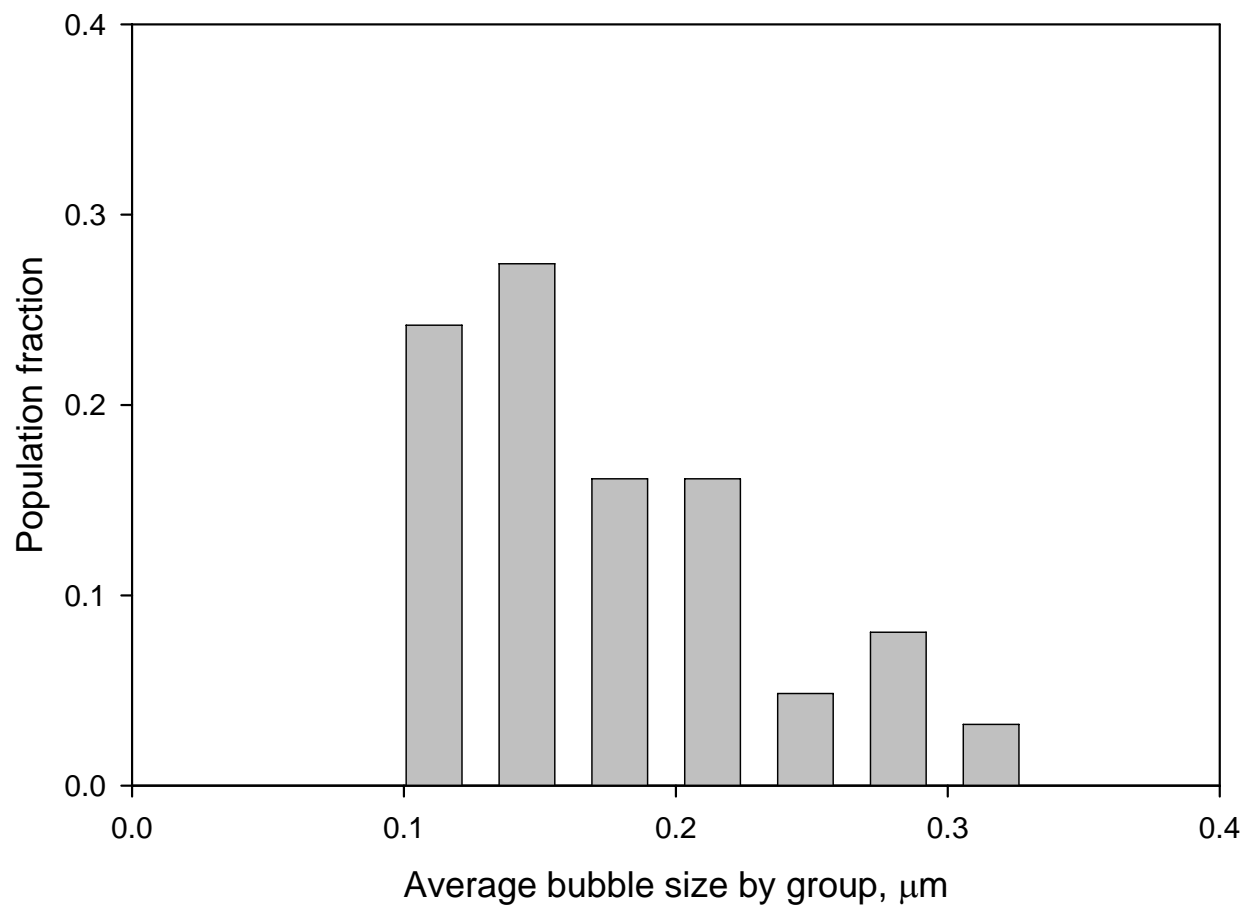
Fig. 16 Bubble size distribution for A003 plate from RERTR-1.
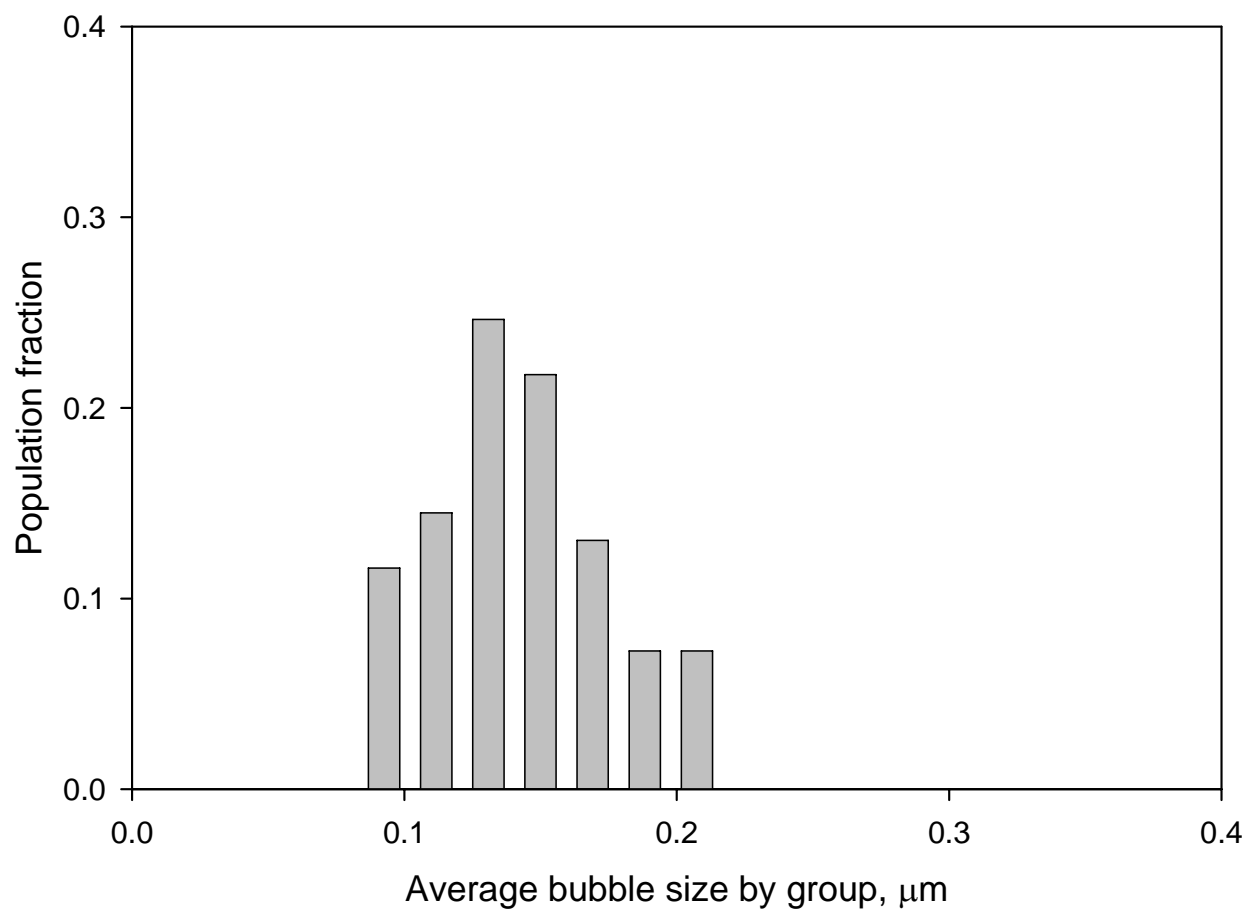
Fig. 17 Bubble size distribution for 580G-V07 plate from RERTR-3.
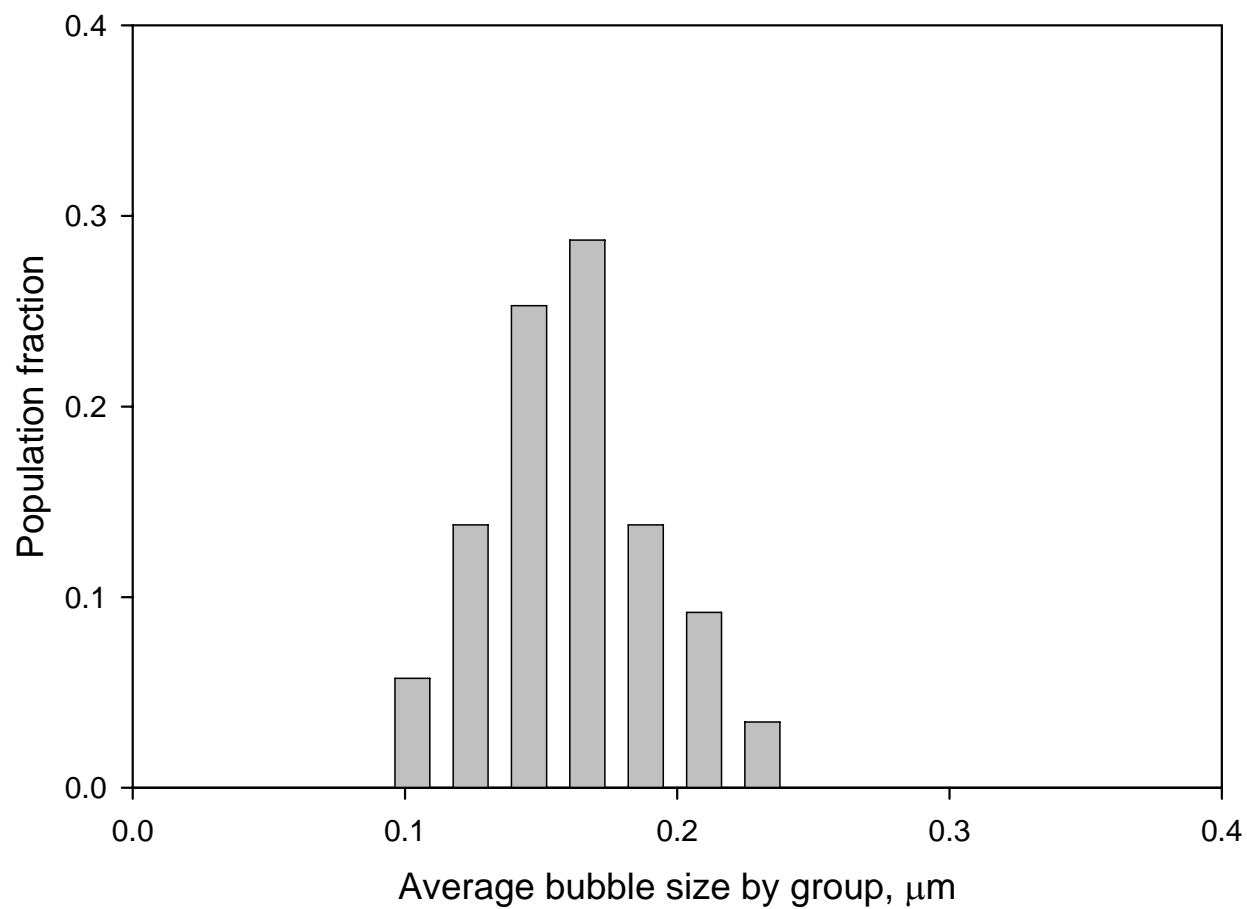
Fig. 18 Bubble size distribution for 580W-V03 plate from RERTR-3.
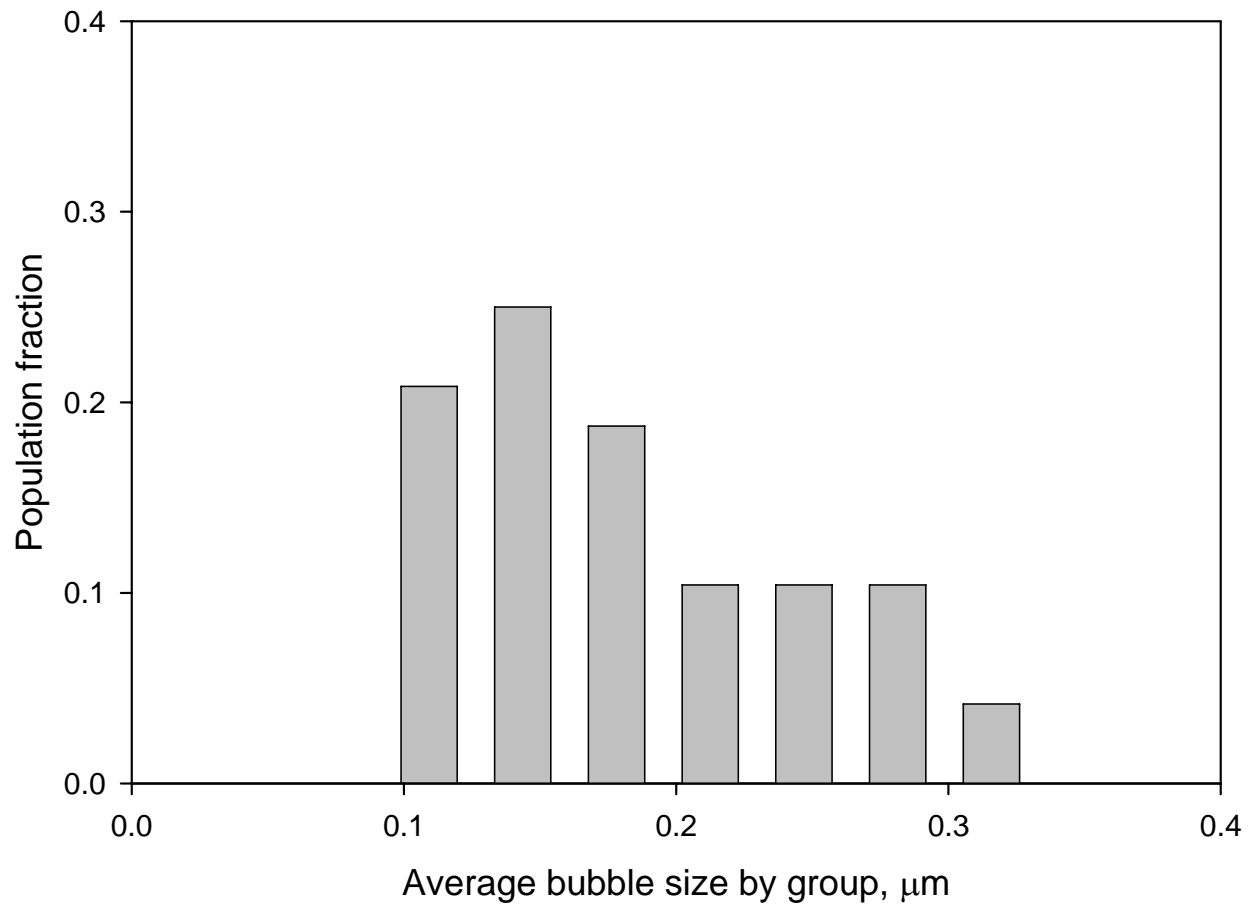
Fig. 19 Bubble size distribution for 580Z-S03 plate from RERTR-3.
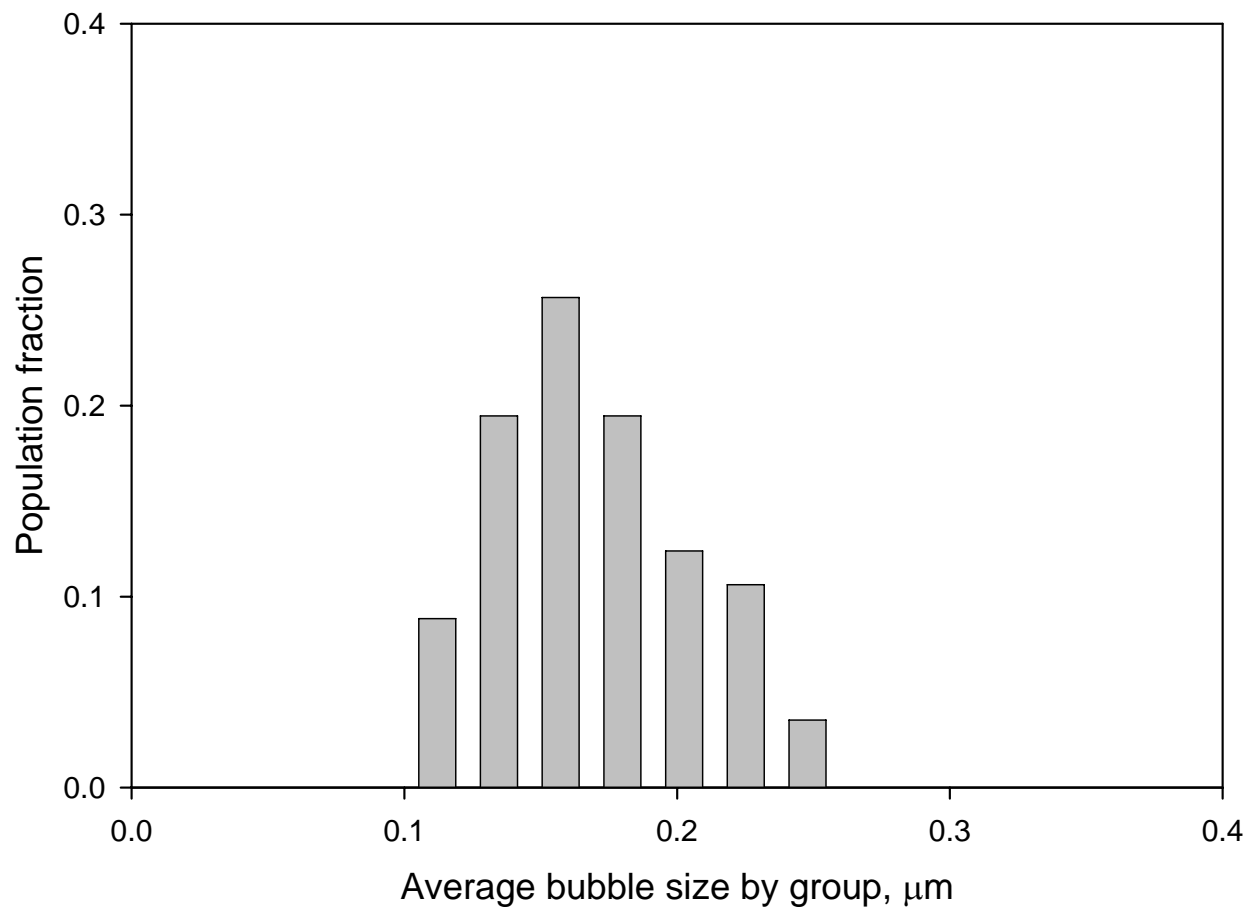
Fig. 20 Bubble size distribution for 600Y-A6008H plate from RERTR-5
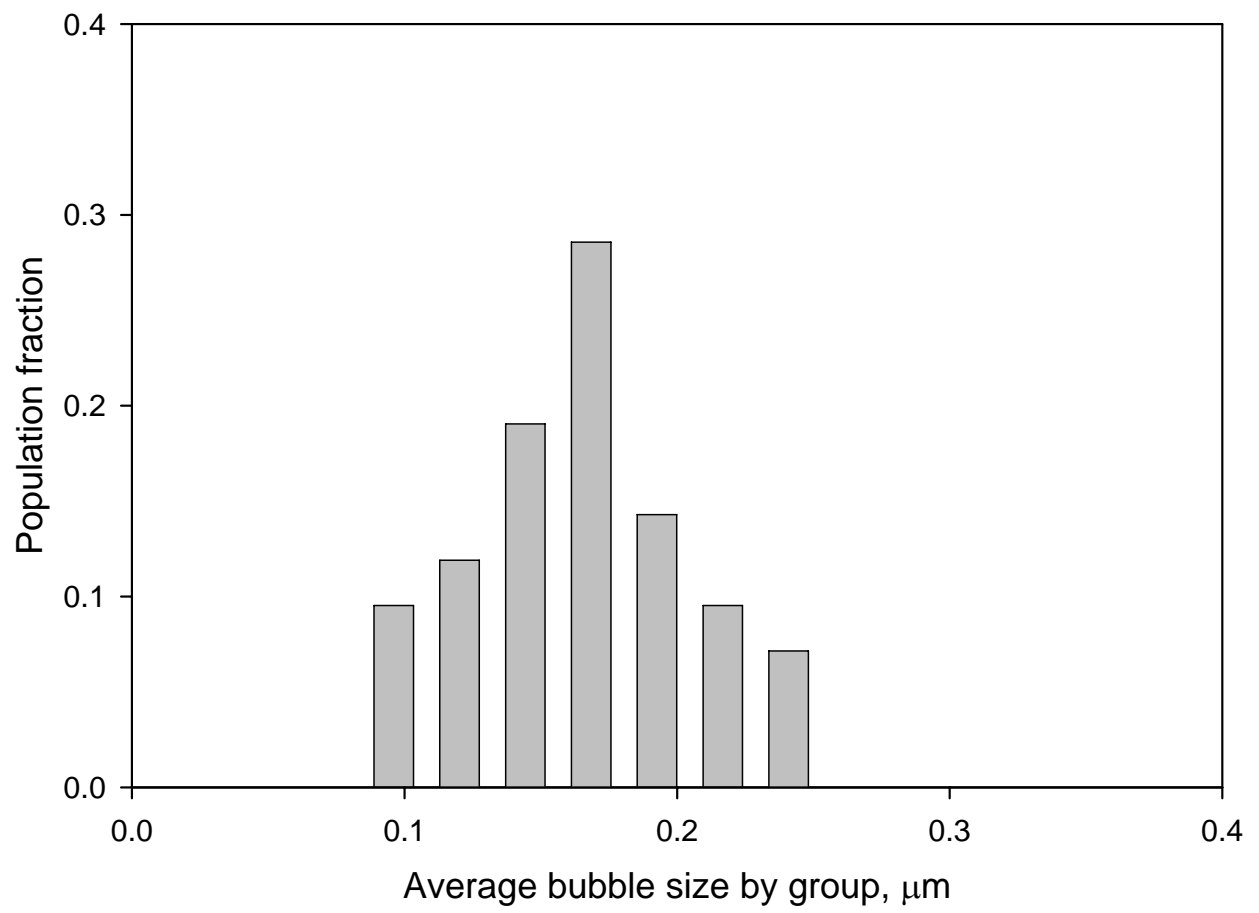
Fig. 21 Bubble size distribution for 600AG-R6007F plate from RERTR-5.
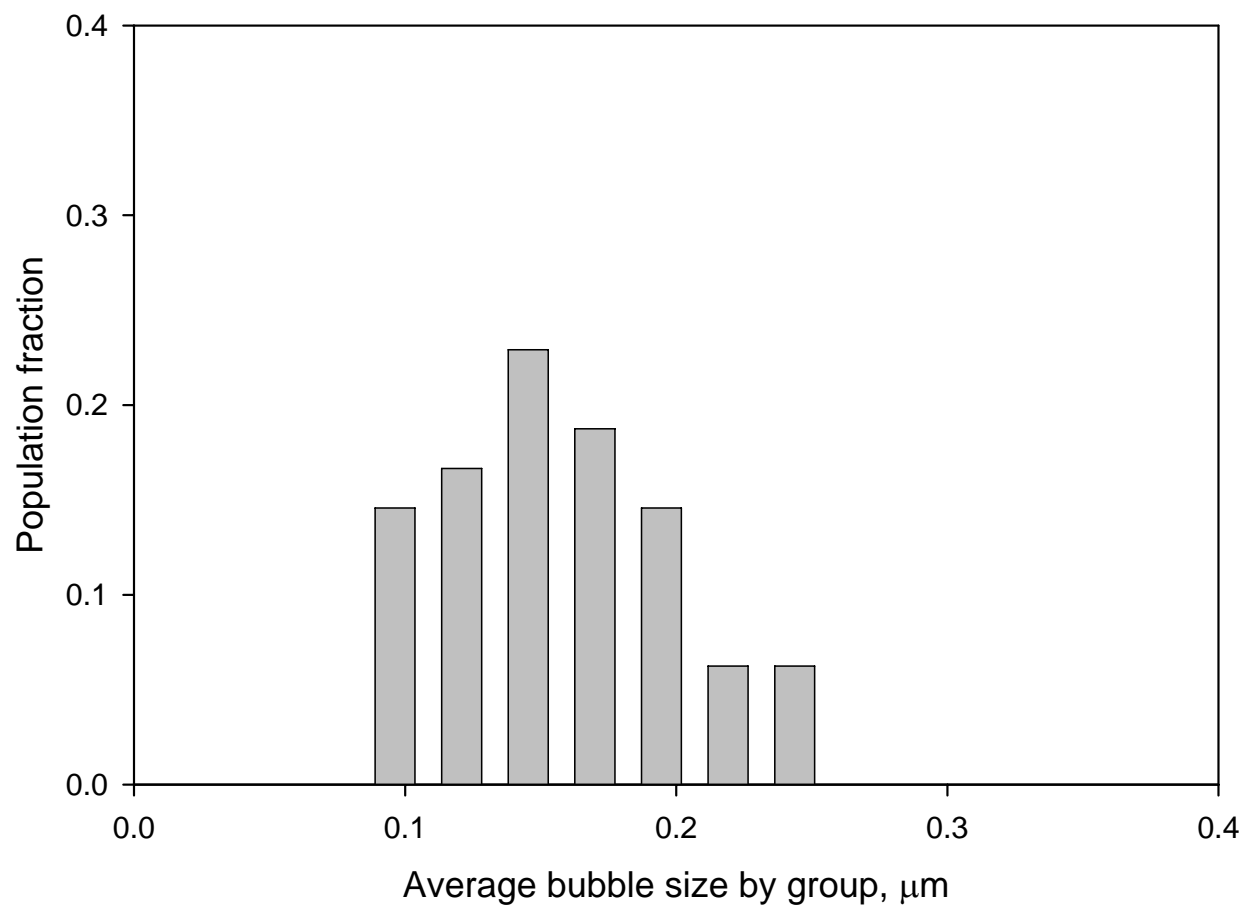
Fig. 22 Bubble size distribution for 600M-V6019G plate from RERTR-5.
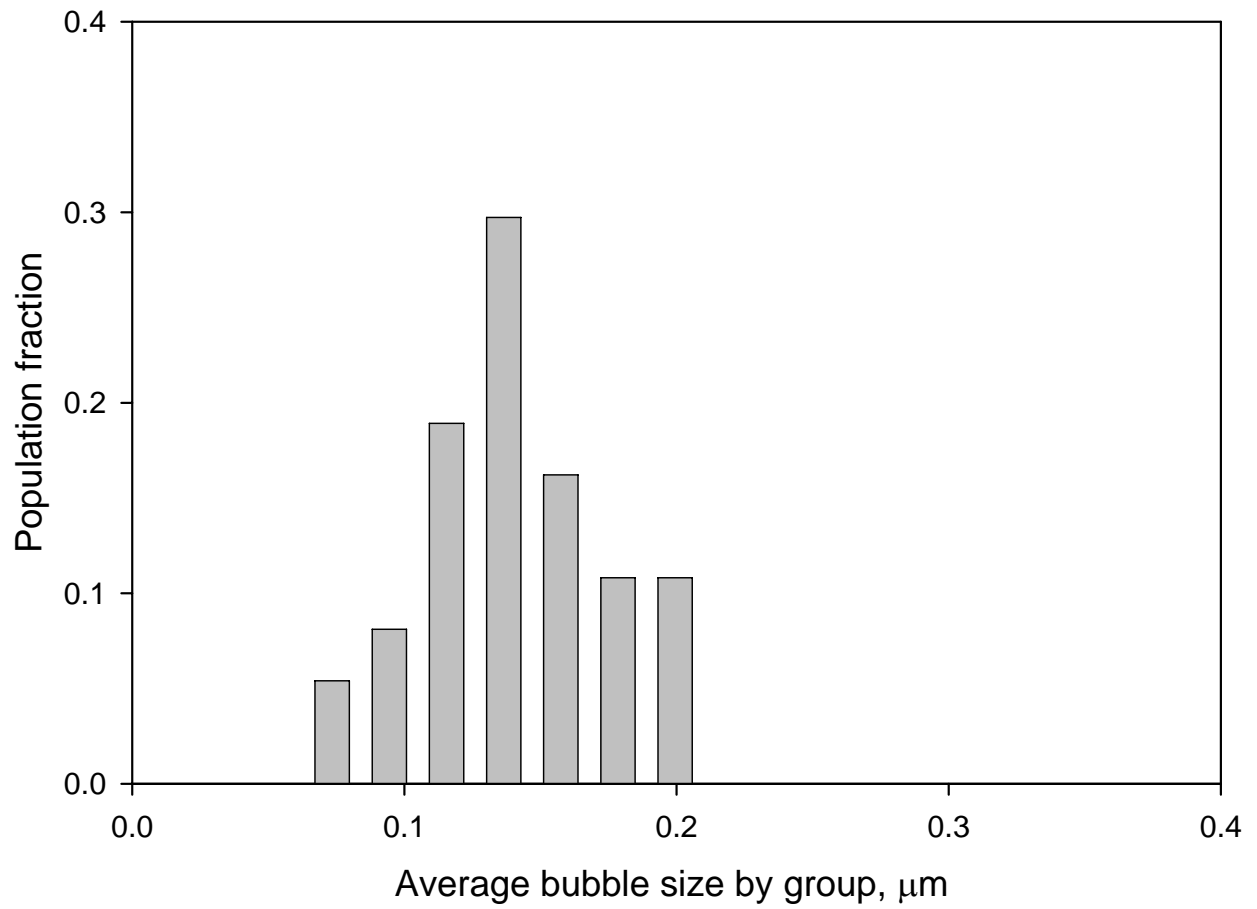
Fig. 23 Bubble size distribution for 600D-V6018G plate from RERTR-5.
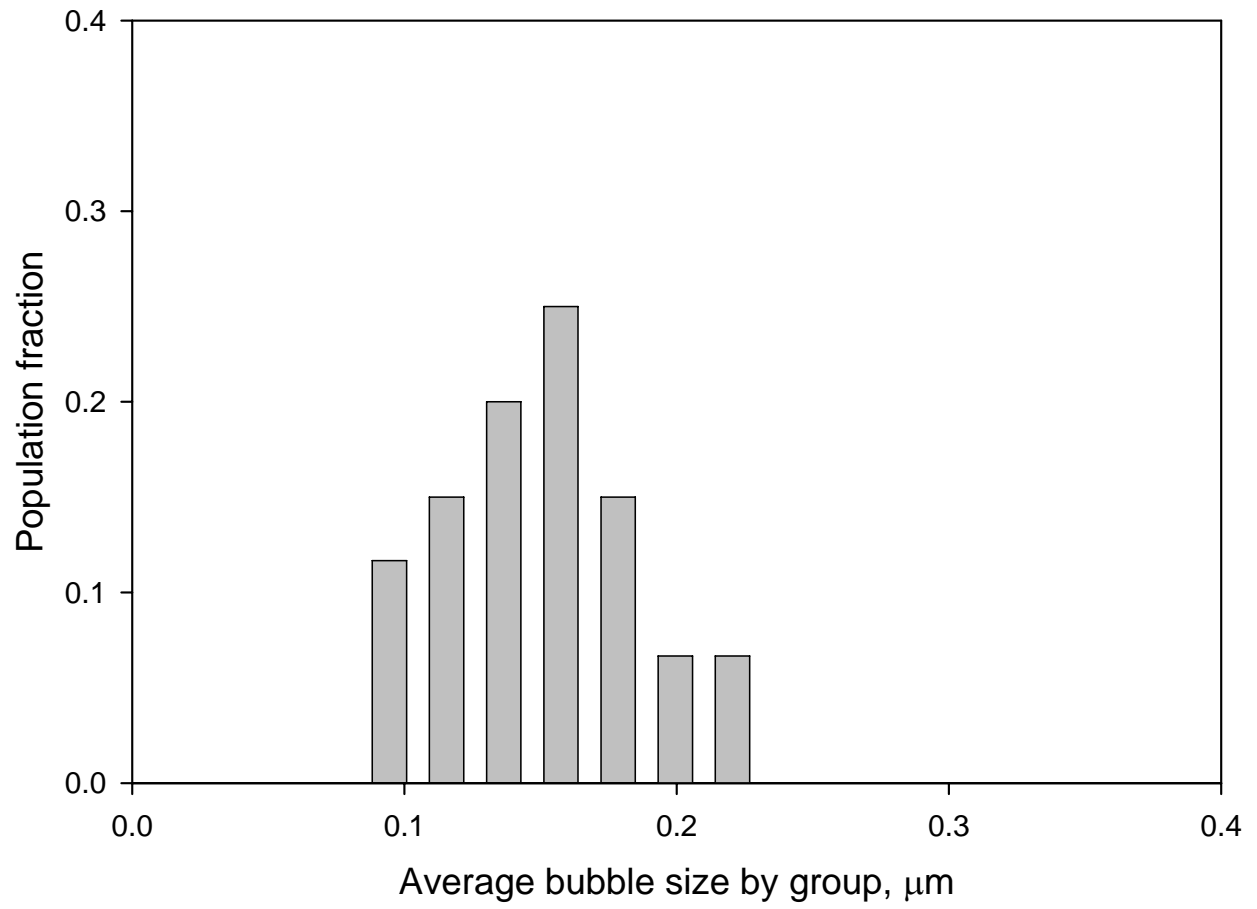
Fig. 24 Bubble size distribution for 600AH-V8005B plate from RERTR-5.
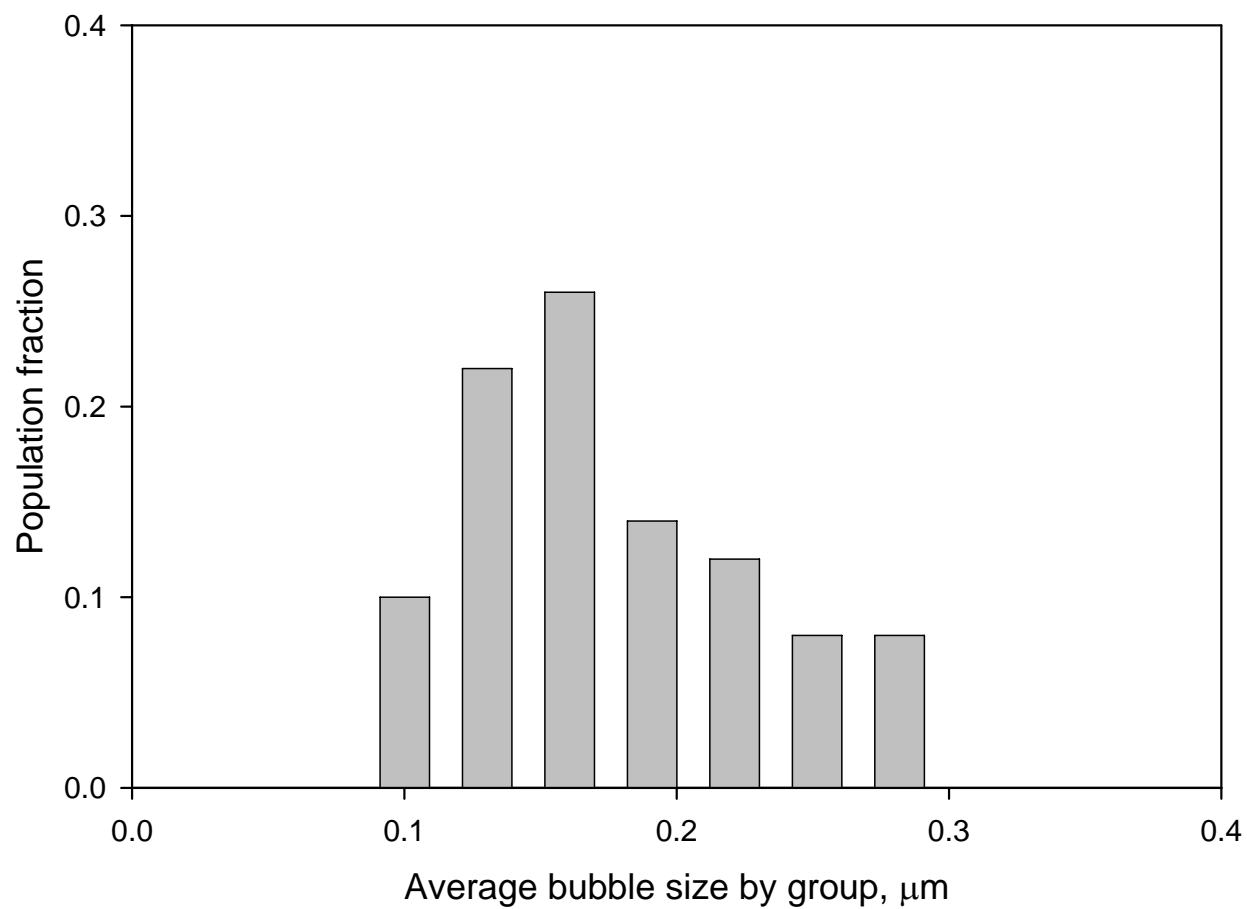
Fig. 25 Bubble size distribution for 600V-A8002L plate from RERTR-5.

Table 3. Average bubble sizes from measurements

Plate ID	Partial recrystallization	Average bubble diameter from measurements, µm
Z03	No	0.09
Y01	No	0.09
V002	No	0.15
A003	No	0.18
V07	No	0.13
V03	No	0.16
S03	Yes	0.18
A6008H	Yes	0.17
R6007F	No	0.16
V6019G	No	0.16
V6018G	No	0.14
V8005B	No	0.16
A8002L	Yes	0.18

In Fig. 26 the average bubble sizes for the plates used in the analysis are shown. Although there are considerable errors, after an initial incubation period the average bubble size increases with fission density and shows saturation at high fission density. As indicated in Table 3, some plates showed the initial stage of recrystallization with signs of multi-layer bubble formation on the grain boundaries. For these plates, the measurement were made on grains not yet affected by recrystallization.
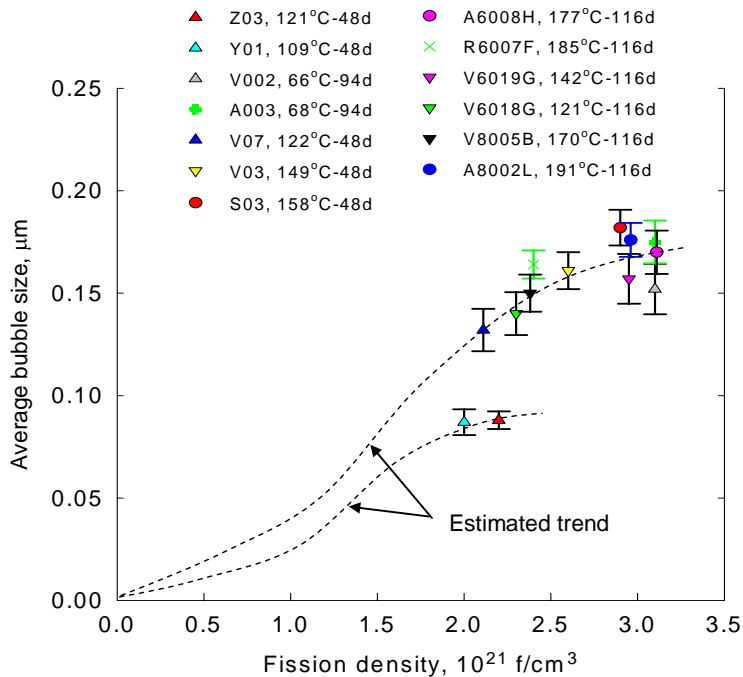
Fig. 26 Measured average bubble size vs. fission density.

3.2 Bubble density analysis

3.2.1 Bubble density per unit grain-boundary length

The bubble populations on grain boundaries were measured on SEM photomicrographs of fractured fuel cross sections as shown in Figs. 8-10. The center-to-center distances between neighboring bubbles were measured. The reciprocal of the average value of the measured distances is equal to the number density per unit grain boundary length, i.e.,

$$\rho_{\mathrm{L}} = \frac{n}{\sum_n \lambda_n} \tag{4}$$

where λ are the distances between bubbles and n is the number of bubbles included in the measurements. The measurement data are given in Table 4.

Some plates with fission densities at or greater than 3×10^{21} f/cm^3 showed the sign of recrystallization. Typically, the appearance of the initial stage of recrystallization is manifested by the formation of multi-layered bubbles on the grain boundaries. For these plates, only grain boundaries with single-layer bubbles were counted in order to catch the bubble characteristics of the pre-recrystallized stage. However, this measurement technique inevitably results in underestimates for bubble volume fractions as compared to those obtained from direct measurement by the point counting method. This will be discussed later in Subsection 3.2.4 and a comparison will be given in Table 8.

Table 4. Measured number of bubbles per grain boundary length

Plate ID	Partial recrystallization	Measured density per unit grain boundary length, ρ_{L}, 10^4 cm^{-1}
Z03	No	1.96
Y01	No	1.79
V002	No	1.30
A003	No	1.41
V07	No	1.34
V03	No	1.36
S03	Yes	1.18
A6008H	Yes	1.43
R6007F	No	1.39
V6019G	No	1.36
V6018G	No	1.32
V8005B	No	1.37
A8002L	Yes	1.35

In Fig. 27, the measured bubble number densities per unit length of grain boundary for all plates are shown. The bubble number densities show no explicit dependence upon fission density. The gamma-annealed powder plates show generally larger values than the as-fabricated powder plates. The machined powder plates also tend to show slightly greater values than the atomized powder plates. The effect of Mo content from this result seems to be negligible considering the measurement error, except perhaps for the lowest Mo content (i.e., 6Mo) of which only a single sample was available.
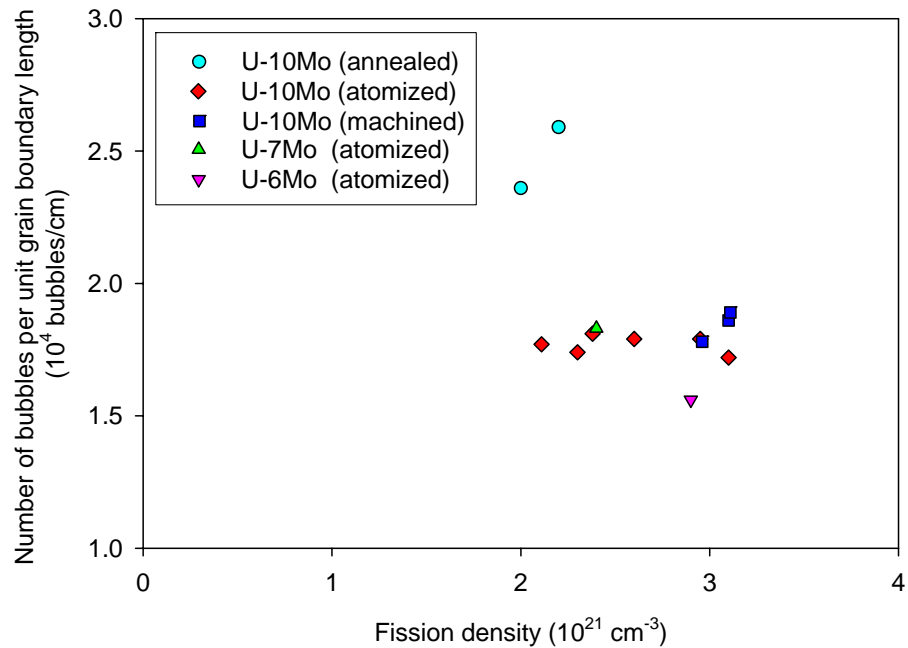
Fig. 27 Number of bubbles per unit length vs. fission density

3.2.2 Bubble density per unit fuel cross section area

Grain size was measured for all plates in the analysis. As discussed in Sect. 2.3, the grain boundaries were discernable because they contain gas bubbles. Two methods were used. The first method is to measure the grain size directly in four different directions of a grain and then calculate the average size by using measurements for several grains from the plate. The second method is the lineal intercept method described in Sect. 2.3. This method is preferable to the direct measurement method. For some plates, no picture was available with good magnification including at least 5 entire grains. In addition, for other plates, the shape of grains was columnar. For this case only one method was used.

It must be mentioned that all grain size measurements were made on SEM images and only a limited number of them were available. Therefore, for some plates, good statistical results could not be obtained because the measurements inevitably included abnormally large or small grains, which could artificially skew the average value. However, bubble measurements were made on these SEM micrographs in order to be consistent for all measurements.

Table 5 gives the summary of the measured grain sizes for the plates used in the analysis. This information is used to obtain number density per unit fuel cross section area and subsequently number density per unit fuel volume.

Table 5. Grain size measurement

Plate ID	Direct measurement		Lineal method
	Grain size, μm	Standard deviation, μm	Grain size, μm
Z03	24.4	9.3	23.6 **
Y01	NM	NM	10.1 *
V002	6.3	0.9	4.9
A003	NM	NM	3.2
V07	NM	NM	6.5
V03	NM	NM	7.3
S03	4.4	NM	3.6
A6008H	5.3	1.3	
R6007F	NM	NM	6.2
V6019G	8.5	3.6	7.6
V6018G	4.9	2	5.2
V8005B	8.1	4.5	NM
A8002L	3.9	1.3	NM

* Machined and annealed, ** Atomized and annealed, NM=Not measured

In order to obtain the bubble volume fraction, the bubble area fraction measured on the fuel cross section is needed. Because bubbles are homogeneously distributed, the bubble volume fraction is equal to the bubble area fraction measured on the cross section [7]. However, our SEM micrographs were taken on fuel fracture surfaces. In the modeling described below, we can convert the bubble density per unit length of grain boundaries to the bubble density per unit cross section area. The bubble area fraction can be obtained by using the average bubble size and bubble density per unit cross section area.

In our model, a grain is modeled as a tetrakaidecahedron (TKDH) [7]. The projection through the center of the TKDH yields a plane as shown in Fig. 28. There are two different kinds of sides with length l and $\sqrt{2}\,l$. The total length of the perimeter (P) and area (S) are:

$$P = 4(1+\sqrt{2}\,)l \tag{5}$$
$$S = 7l^2 \tag{6}$$

The bubble number density per unit area on this projected plane from the measured number density per unit length, ρ_{cs}, can be obtained by

$$\rho_{CS} = \frac{1}{2}\frac{P}{S}\rho_L \tag{7}$$

where ρ_L is the measured bubble density per unit length given in Table 4. The factor ½ in front of the equation takes into account that every side of TKDH is shared by a neighboring grain.
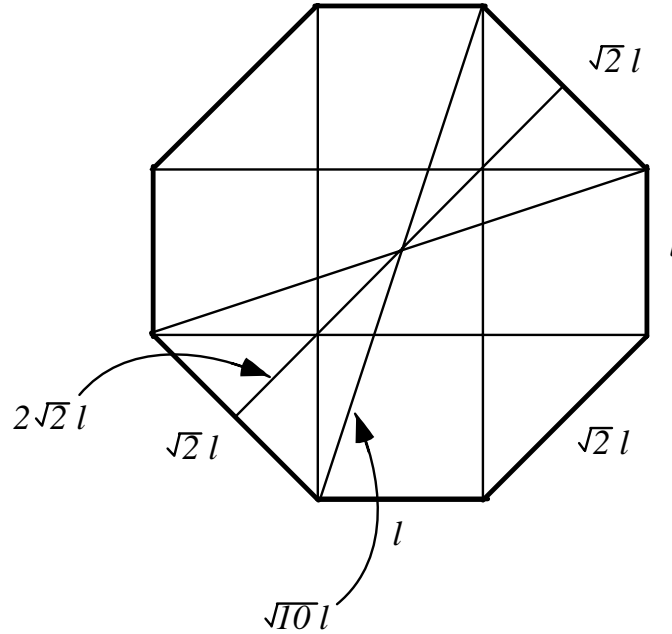
Fig. 28 Tetrakaidecahedron (TKDH) modeling of grain cross section.

Substituting Eqs. (5) and (6) in Eq.(7) gives

$$\rho_{CS} = \frac{2 \cdot (1 + \sqrt{2})}{7 \cdot l} \rho_L \tag{8}$$

The diagonal length varies between $2\sqrt{2}\, l$ and $\sqrt{10}\, l$, as shown in Fig. 28. Taking the average of this and setting the grain size equal to the diagonal length, we obtain d=3l where d is the grain size. Therefore, Eq. (8) becomes

$$\rho_{CS} = \frac{6 \cdot (1 + \sqrt{2})}{7 \cdot d} \rho_L \tag{9}$$

The data for the bubble density per unit grain boundary length are given in Fig. 27. Using Eq. (9), the calculated density data per unit fuel cross section area for all plates are presented in Table 6 and plotted in Fig. 29.

Using Eq. (9), we obtain the grain boundary length per unit fuel cross section area, L^*.

$$L^* = \frac{\rho_{CS}}{\rho_L} = \frac{6 \cdot (1 + \sqrt{2})}{7 \cdot d} \tag{10}$$

Figure 30 shows the results for L*. The symbols are the measured values and the line is the calculated by using the TKDH model. Good agreement between the measured and calculated shows that the application of the TDKH model is valid.

Table 6. Number of bubbles per unit fuel cross section area converted from the
measured bubble number per unit grain boundary length data

Plate ID	Partial recrystallization	Measured density per unit grain boundary length, ρ_L, 10^4 cm^{-1}	Calculated density per unit fuel cross section area, ρ_{cs}, 10^8 cm^{-2}
Z03	No	1.96	0.17
Y01	No	1.79	0.36
V002	No	1.30	0.55
A003	No	1.41	0.92
V07	No	1.34	0.43
V03	No	1.36	0.39
S03	Yes	1.18	0.67
A6008H	Yes	1.43	0.56
R6007F	No	1.39	0.46
V6019G	No	1.36	0.37
V6018G	No	1.32	0.53
V8005B	No	1.37	0.35
A8002L	Yes	1.35	0.72
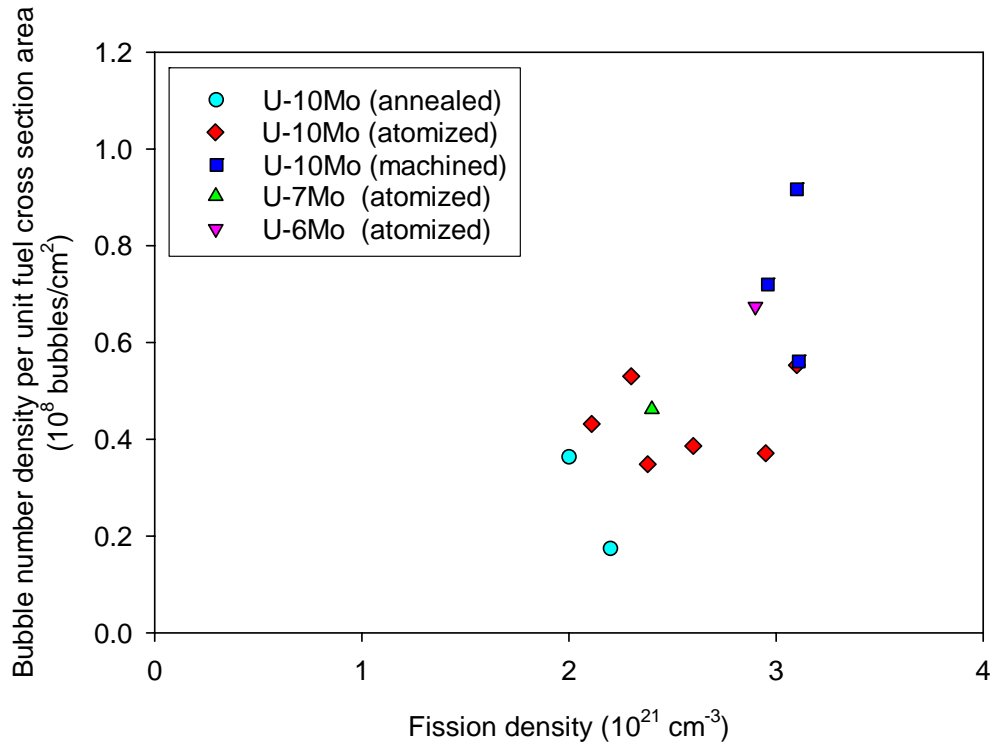
Fig. 29 Number of bubbles per unit fuel cross section area calculated from ρ_L.
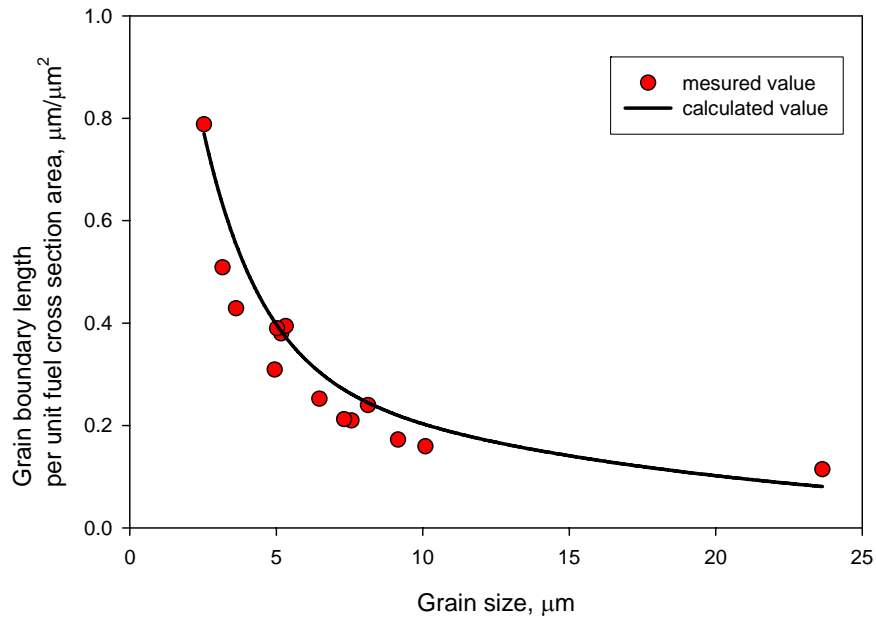
Fig. 30 Comparison between the measured and calculated grain boundary length per unit fuel cross section area vs. grain size.

3.2.3 Bubble density per unit grain surface area

We assume that the bubbles on the grain surfaces of a TKDH are uniformly distributed. Thus, we model the distribution as a close-packed array as shown in Fig. 31. Each bubble occupies an equal amount of the circular surface area with diameter D with the border line depicted by the dashed line. As can be seen, there is some non-occupied area; we call this 'empty area.' In this model, the distance between two neighboring bubbles from center to center is also D.
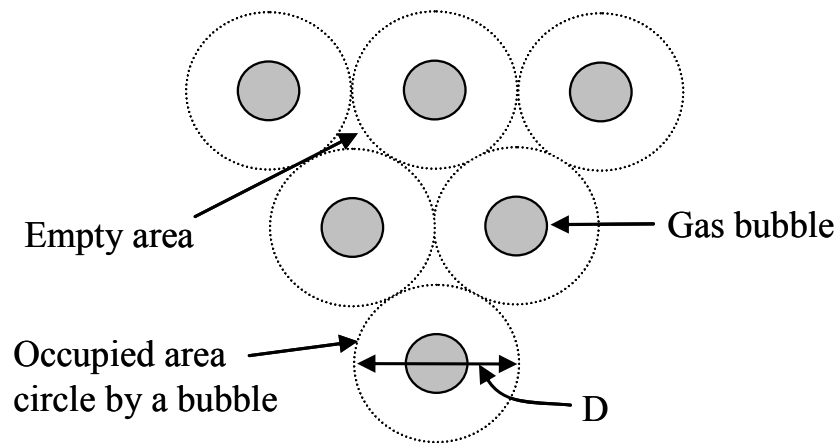
Fig. 31 Schematic of the model used for bubble distribution analysis on the grain surface.

In this model, the bubble density per unit surface area is the reciprocal of the specific area for a bubble. The specific area consists of the area of the circle with diameter D, and the sum of two empty areas shown in Fig. 31. The area of a circle (S_c) is

$$S_c = \frac{\pi \cdot D^2}{4} \tag{11}$$

The area of an empty area (S_e) is

$$S_e = \frac{(2 \cdot \sqrt{3} - \pi)}{2} \cdot \frac{D^2}{4} \tag{12}$$

Thus, the area of a bubble (S_b) is

$$S_b = \frac{\sqrt{3}}{2} \cdot D^2 = \frac{\sqrt{3}}{2} \frac{1}{\rho'_L{}^2} \tag{13}$$

where ρ'_L is the average bubble density per unit grain boundary length measured on the grain surface. This quantity is usually different from that measured on the grain boundaries. This will be discussed later in this Section.

Therefore, the density per unit grain surface area is

$$\rho_S = \frac{1}{S_b} = \frac{2}{\sqrt{3}} \rho'_L{}^2 \tag{14}$$

The relationship between ρ'_L and ρ_L needs to be known in order to use Eq. (14) because ρ_L are the known data from the measurements, which are given in Table 4. We model the bubbles on the grain surface as distributed in a close-packed plane, as shown in Fig. 32. The average distance between two bubbles on the grain boundaries exposed on the cross section is usually *larger* than that measured on the real grain surface (see Fig. 32) because the cross section is not necessarily made on the close-packed line (solid line in Fig. 32). The solid line in Fig. 32 shows the close-packed line of bubbles, whereas the broken lines show the possible grain boundaries on a cross section having greater distances between bubbles than those on the solid line. As a result, the measured bubble number density per unit grain boundary length measured on a cross section is less than that measured on a real grain surface.
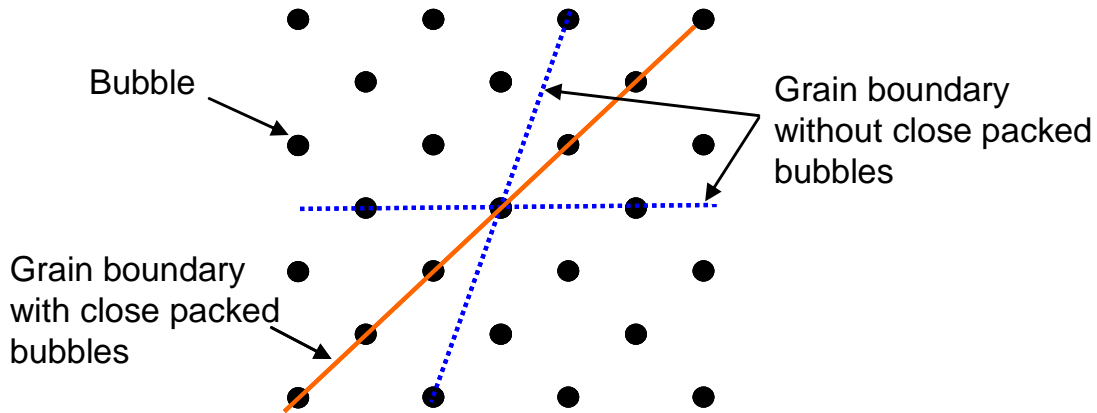
Fig. 32 Schematic of possible grain boundary bubble configurations on cross section.

36

In addition, as can be seen in the SEM photos in Figs. 8 - 10, the grain boundaries are rarely straight lines. There are many turns visible on the grain boundaries, suggesting that the grain boundaries are composed of many combinations of possible distances between two bubbles as shown in Fig. 32. Therefore the distance between two bubbles is a statistical average considering all possible combinations of bubble configuration. Thus, a model to modify the measured values of bubble number density per unit grain boundary length on a cross section for real values is necessary.

In Fig. 33, let the center-to-center distance between O and B_1, that between O and B_2, and that between O and B_3 be d_1, d_2, and d_3, respectively. The probability that a cross section is cut through two bubbles on one of these three cases is inversely proportional to the square of the distances between two bubbles. Thus, considering the three most probable cases that can be exposed on a cross section surface; O and B_1, O and B_2, and O and B_3, the average surface-to-surface distance between two bubbles on a cross section can be expressed as

$$\bar{\delta} = \frac{A}{d_1^2} \cdot \delta_1 + \frac{A}{d_2^2} \cdot \delta_2 + \frac{A}{d_3^2} \cdot \delta_3 \tag{15}$$

where A/d_1^2, A/d_2^2, and A/d_3^2 are the probabilities that the cross section is cut through O and B_1, O and B_2, and O and B_3, respectively, where A is an arbitrary constant and δ_1, δ_2, and δ_3 are the surface-to-surface distances between O and B_1, O and B_2, and O and B_3, respectively.
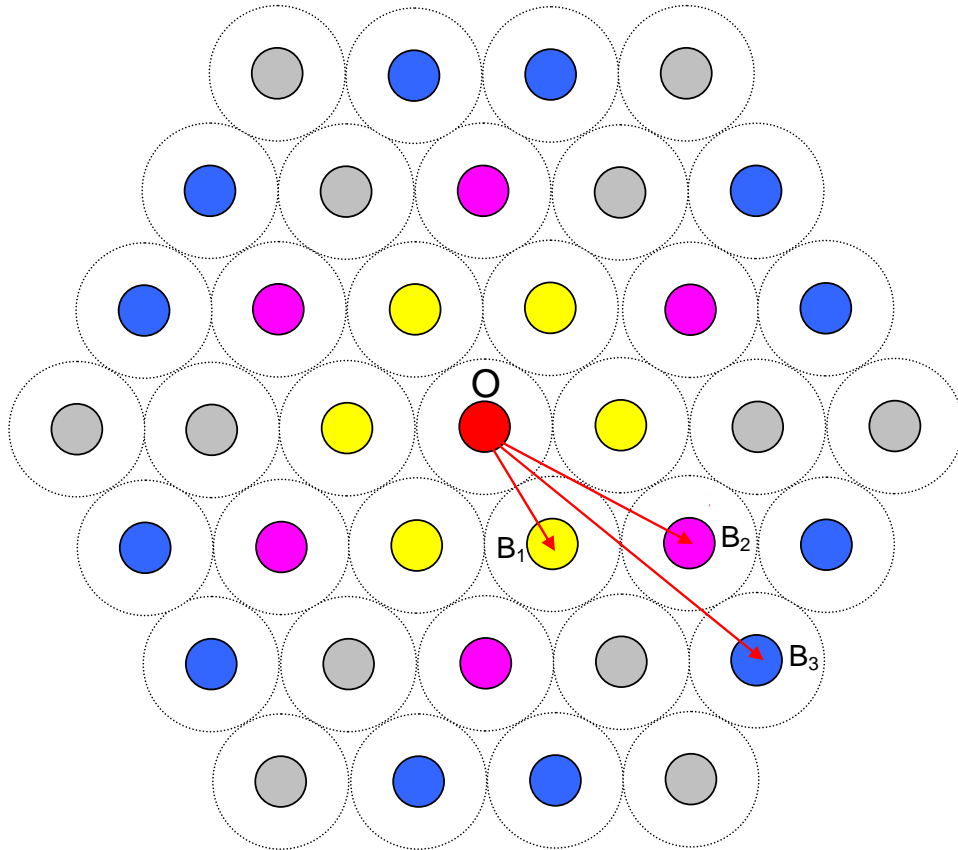
Fig. 33 Schematic showing the method to determine the average distance between bubbles.

It can be shown that $d_1=D$, $d_2 = \sqrt{3}\,D$, and $d_3 = \sqrt{7}\,D$ where D is the distance between the centers of two nearest bubbles shown in Fig. 32. Then, Eq. (15) becomes

$$\bar{\delta} = \frac{A}{D^2} \cdot (\delta_1 + \frac{1}{3}\delta_2 + \frac{1}{7}\delta_3) \tag{16}$$

Since the sum of probabilities of all three cases is unity, i.e.,

$$\frac{A}{d_1^2} + \frac{A}{d_2^2} + \frac{A}{d_3^2} = 1 \tag{17}$$

we have

$$A = \frac{D^2}{1+\dfrac{1}{3}+\dfrac{1}{7}} \tag{18}$$

Substituting Eq. (18) in Eq. (16) gives

$$\bar{\delta} = \frac{1}{1+\dfrac{1}{3}+\dfrac{1}{7}} \cdot (\delta_1 + \frac{1}{3}\delta_2 + \frac{1}{7}\delta_3) \tag{19}$$

Using $\delta_1=D-x_0$, $\delta_2 = \sqrt{3}\,D - x_0$, $\delta_3 = \sqrt{7}\,D - x_0$ where x_0 is the average bubble size, we can rearrange Eq.(19) as

$$\bar{\delta} = \frac{(1+\dfrac{1}{\sqrt{3}}+\dfrac{1}{\sqrt{7}})}{1+\dfrac{1}{3}+\dfrac{1}{7}} \cdot D - x_0 \tag{20}$$

Since, by definition, $\rho_L = 1/(\bar{\delta} + x_o)$ and $\rho'_L = 1/D$, $\bar{\delta} = 1/\rho_L - x_0$ and $D = 1/\rho'_L$. Substitution of these equalities in Eq. (20) gives

$$\rho'_L = \frac{(1+\dfrac{1}{\sqrt{3}}+\dfrac{1}{\sqrt{7}})}{1+\dfrac{1}{3}+\dfrac{1}{7}} \rho_L \tag{21}$$

The term in front of ρ_L in Eq. (21) has a value of 1.32, meaning that the measured values are about 32% lower than the real values.

By using Eqs. (14) and (21), the density per unit grain surface area can be calculated from the measured ρ_L given in Table 4. The results are provided in Table 7 and shown in Fig. 34. Because ρ_L is independent on fission density, ρ_S, which is a is a function of only ρ_L, is also independent on fission density.

38

Table 7. Calculated and measured number of bubbles per unit grain surface area (ρ_S)

Plate ID	Calculated, 10^8 cm^{-2}	Measured, 10^8 cm^{-2}	Measured / calculated
Z03	13.6	NM	NA
Y01	11.3	NM	NA
V002	6.0	NM	NA
A003	7.0	NM	NA
V07	6.4	NM	N
V03	6.5	NM	NA
S03	5.0	4.6	0.93
A6008H	7.3	4.9	0.67
R6007F	6.1	7.2	1.2
V6019G	6.5	NM	NA
V6018G	6.1	5.9	0.97
V8005B	6.6	NM	NA
A8002L	6.4	NM	NA

NM = Not measured, NA = Not available
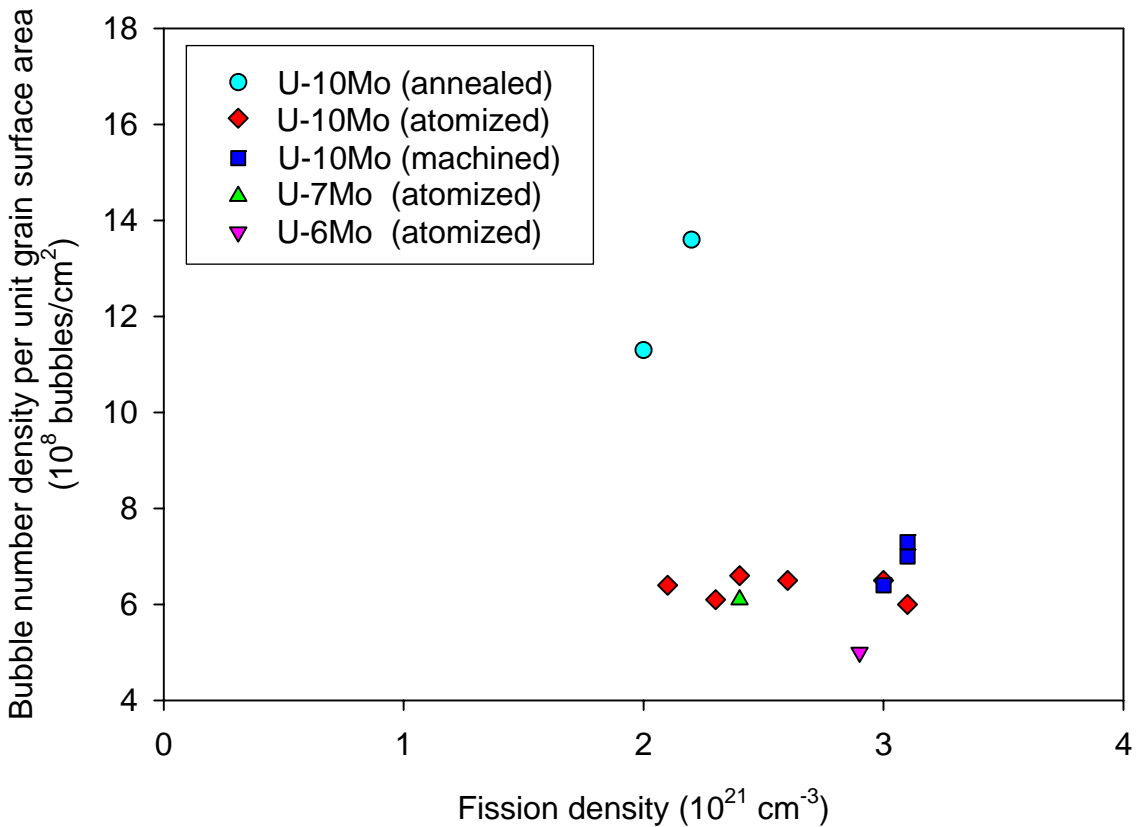
Fig. 34 Number of bubbles per unit grain boundary surface area vs. fission density

We also directly measured the bubble density on some exposed grain surfaces (see Fig. 35) for several plates. The results are also included in Table 7. The comparison between the measured and the calculated show good agreement.
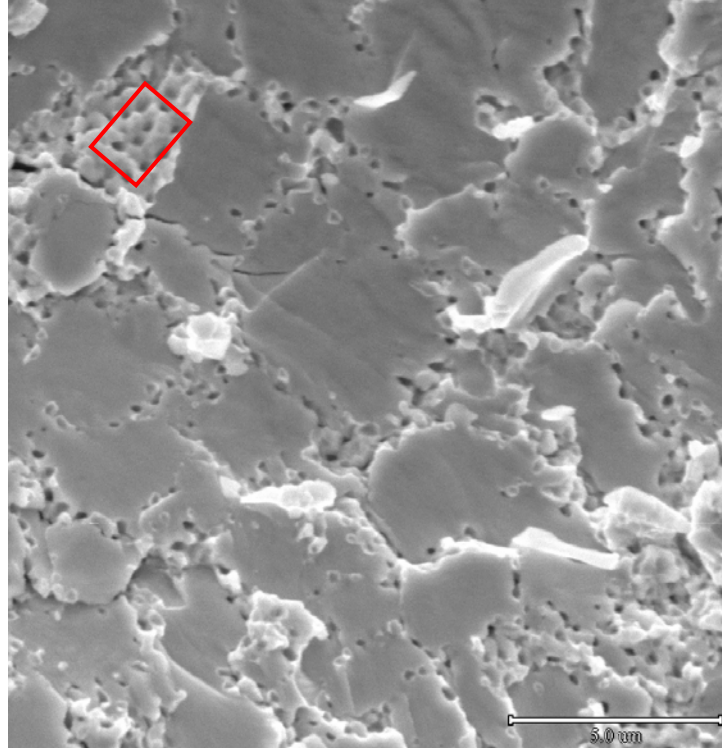
Fig. 35 SEM photo of A6008H (600Y) from RERTR-5 showing an example of surface area bubbles. The red marker is for the area the bubble density was measured.

3.2.4 Bubble density per unit fuel volume

The bubble density per unit fuel volume can be obtained by considering the surface-to-volume ratio of the TDKH. The volume of a TDKH is

$$V_{TDKH} = 8 \cdot \sqrt{2} \cdot l_0^3 \qquad (22)$$

where l_0 is the edge length and approximately equal to $(1/3)d$ where d is the average size of the TDKH.

The surface area of the TDKH is

$$S_{TDKH} = 6 \cdot (1 + 2\sqrt{3}) \cdot l_0^2 \qquad (23)$$

By using Eqs. (22) and (23) we obtain a relation between the cross section surface and volume density:

$$\rho_V = \frac{1}{2} \cdot \frac{S_{TDKH}}{V_{TDKH}} \rho_S \qquad (24)$$

or

$$\rho_V = \frac{9(1+2\sqrt{3})}{8\sqrt{2}\cdot d}\rho_S \qquad (25)$$

where ρ_S is the bubble density per unit grain surface area given by Eq. (14).

The bubble density per unit fuel volume is calculated using Eqs. (14) and (25), and is shown in Fig. 36 and given in Table 8. Figure 36 shows that, although not obvious, the lower Mo-content plates show higher bubble volume fractions. This means that the lower Mo-content plates show higher fuel swelling. This observation is subject to the theoretical modeling described in Section 4.
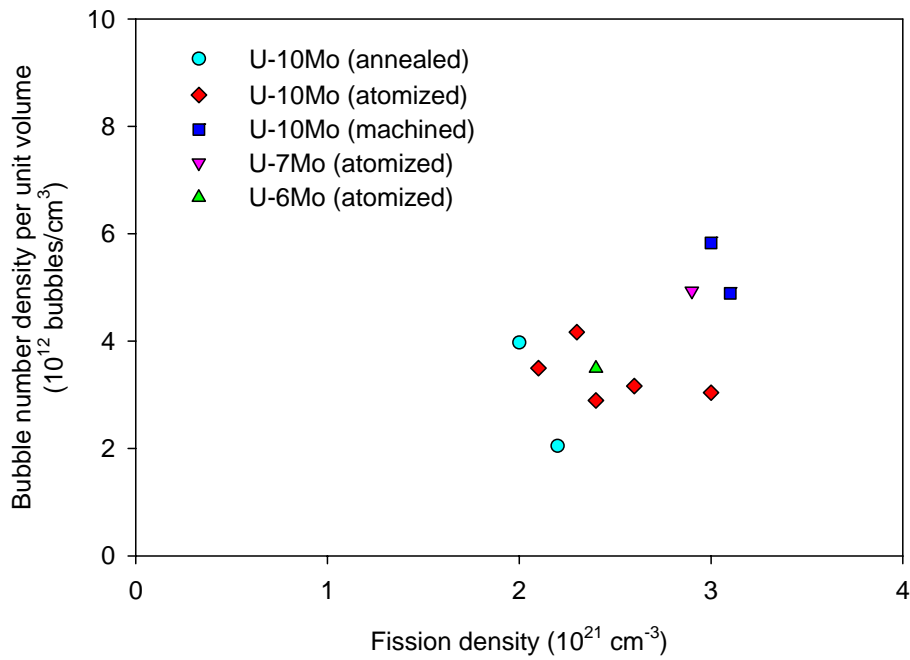
Fig. 36 Number of bubbles per unit fuel volume calculated from ρ_S.

3.3 Gas bubble volume fraction and fission gas swelling

The total gas bubble (i.e., observable bubble) volume fraction in fuel can be calculated as follows:

$$v_b = \frac{\pi \cdot x_o^{3}}{6}\rho_V \qquad (26)$$

where v_b is the gas bubble volume fraction in the fuel.

Bubble volume fraction, v_b, can also be given by

$$v_b = \frac{\pi \cdot x_o^2}{4} \rho_{CS} \tag{27}$$

where ρ_{CS} is the bubble density per unit fuel cross section area from Table 6 and x_0 is the average bubble size from Table 3. In Eq. (27), the fact that the bubble volume fraction is equal to the bubble area fraction is used [7]. The gas bubble volume fractions are calculated using ρ_S and ρ_{CS} from Eqs. (26) and (27), and are given in Table 8.

Table 8. Gas bubble volume fractions

Plate ID	Fission density, 10^{21} f/cm^3	Partial Recrystall- ization	ρ_V calculated from ρ_S, 10^{12} cm^{-3}	v_b calculated from ρ_S, %	v_b calculated from ρ_{CS}, %	v_b measured * %
Z03 (a-γ)	2.2	No	2.0	0.1	0.1	0.2
Y01 (m-γ)	2.0	No	4.0	0.2	0.2	NM
V002 (a)	3.1	No	4.3	0.8	1.0	1.2
A003 (m)	3.1	No	7.8	2.4	2.3	2.7
V07 (a)	2.1	No	2.5	0.8	0.6	NM
V03 (a)	2.6	No	3.5	0.4	0.8	NM
S03 (a)	2.9	Yes	3.2	0.7	1.7	2.0
A6008H (m)	3.1	Yes	4.9	1.5	1.3	NM
R6007F (a)	2.4	No	4.9	1.3	0.9	1.6
V6019G (a)	3.0	No	3.5	0.7	0.7	2.0
V6018G (a)	2.3	No	3.0	0.7	0.8	NM
V8005B (a)	2.4	No	4.2	0.6	0.7	NM
A8002L (m)	3.0	Yes	2.9	0.6	1.8	3.2

a: atomized powder, m: machined powder, γ: γ-phase annealed powder,
* Measured by point counting, NM = Not measured

The direct volume analysis method, i.e., the point counting method, was used to obtain the bubble volume fractions for several plates. The point counting method converts the area fraction occupied by the bubbles on a SEM photo to the gas bubble volume fraction. This verification method allows a direct measurement of the volume fraction from the area fraction occupied by bubbles on the cross section. The results calculated from ρ_{CS} show better consistency than those from ρ_S when compared with the point counting results.

In general, all three methods are fairly consistent with some exceptions. The plates with inconsistent results are all from the partially recrystallized plates. The values from ρ_{CS} are larger than those from ρ_S, and are more consistent with the direct measurement values. The values from the direct measurement are the largest of all. All of these observations point toward the argument that the inconsistencies originated from the measurement of ρ_L that excluded the

partially recrystallized regions on the fuel cross sections, whereas the calculated values from ρ_{CS} and the direct measurements included those regions that have more populated bubbles, as discussed in Subsection 3.2.1.

The machined plates have consistent results for all three methods. The machined powders have more equiaxial shaped grains and a more homogeneous distribution of grains than the atomized powder fuel because there is no thermal process involved during fabrication. This allows for a more accurate grain size measurement. In atomized particles, however, the grains are typically in columnar shapes at the particle periphery, and more isotropic in shape at the particle interior and larger in size than those at the periphery. Because we use high magnification SEM photos, the measurements are frequently localized and dependent on the fracture direction resulting in errors in grain size measurements.

The calculated results for gas bubble volume fraction using the bubble density per unit cross section area are shown in Fig. 37. The bubble volume fraction, which is equal to fission gas bubble swelling, is a function of fission density. The lower Mo-content fuel plates show slightly higher bubble volume fractions. This also suggests fuel swelling is dependent on the Mo content, although an exact quantification is not available for the present work.
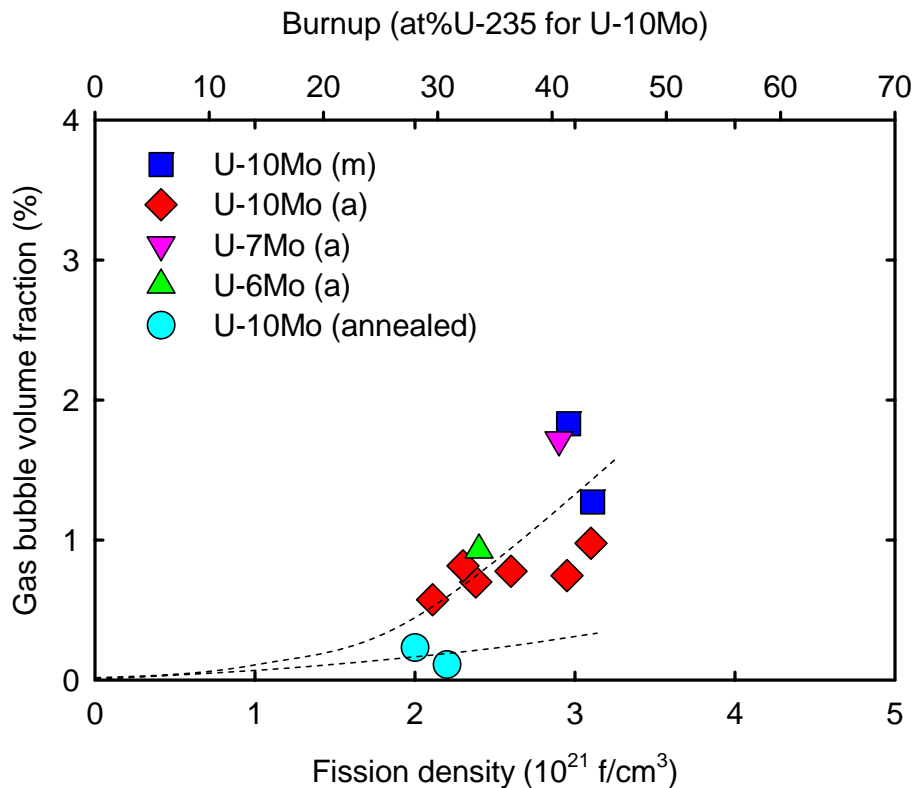
Fig. 37 Gas bubble volume fraction calculated from ρ_{CS}.

The fuel swelling data based on plate thickness measurements before-and-after the irradiation tests are shown in Fig. 38 [9]. A linear fit gives total fuel swelling (%) as

$$\left(\frac{\Delta V}{V_0}\right)_{total} = 6 \times 10^{-21} F_d \tag{28}$$

The solid fission product swelling and intragranular fission gas bubble contribution to swelling is the difference between the total swelling and the measured gas bubble swelling.

Fission gas bubble swelling was obtained by using the gas bubble volume fraction data shown in Fig. 37. Modification to reflect the initial fuel volume by multiplying by $(1+(\Delta V/V_0)_s)$ was made where $(\Delta V/V_0)_s$ is the fuel matrix swelling obtained by subtracting the gas bubble swelling from the total swelling. The result is shown in Fig. 38. The plate thickness data of monolithic fuel plates and dispersion fuel plates with Si-modified matrixes, for which the thickness increase is due to fuel swelling, are used to obtain the total swelling.
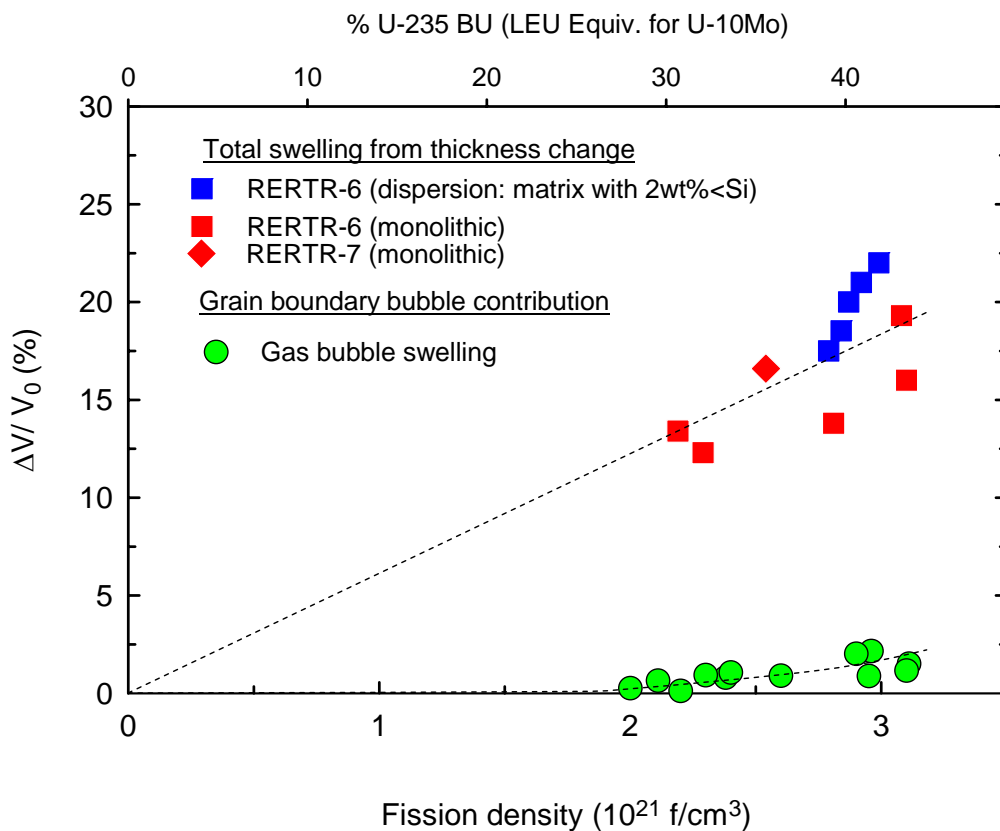
Fig. 38 Comparison of total fuel swelling assessed from plate thickness changes and contribution by intergranular gas bubble swelling.

Figure 38 shows that the contribution to the total swelling by fission gas bubbles is very small. This suggests that in the pre-transition regime a considerable concentration of fission gas remains in atomic solution or in small bubbles not resolvable by SEM.

4. Mechanistic model development

4.1 Calculation of evolution of average intra and intergranular bubble-size and density

The model presented here considers analytical solutions to coupled rate equations that describe the nucleation and growth of inter- and intragranular bubbles under the simultaneous effect of irradiation-induced gas-atom re-solution. The goal of the formulation is to avoid a coupled set of nonlinear equations that can only be solved numerically, using instead a simplified, physically reasonable hypothesis that makes the analytical solutions viable. The gas-induced swelling rate is then assessed by calculating the evolution of the bubble population with burn-up and subsequently the amounts of gas in bubbles and lattice sites. Uncertain physical parameters of the model are adjusted by fitting the calculated bubble populations at given burn-ups with measured bubble size and density data.

At the irradiation temperatures of interest (T < 500K), the diffusion of fission gas atoms is athermal and proportional to the fission rate, $\dot{f}$ (fissions·cm^{-3}·s^{-1}), and the gas-atom diffusion coefficient, D_g, is given by

$$D_g = D_0 \dot{f} \tag{29}$$

In general, the gas-atom re-solution rate is also proportional to the fission rate, i.e.,

$$b = b_0 \dot{f} \tag{30}$$

Within the content of mean field theory, the rate equation describing the time evolution of the density of gas in intragranular bubbles is given by

$$\frac{d[m_b(t)c_b(t)]}{dt} = 16\pi f_n D_g r_g c_g(t)c_g(t) + 4\pi r_b(t)D_g c_g(t)c_b(t) - bm_b(t)c_b(t) \tag{31}$$

The three terms on the right hand side of Eq. (31) represent, respectively, the change in the density of gas in intragranular bubbles due to bubble nucleation, the gas-atom diffusion to bubbles of radius, r_b, and the loss of gas atoms from bubbles due to irradiation induced re-solution. Equation (31) can also be represented as the sum of two equations denoting, respectively, the time evolution of the fission gas bubble density c_b and of the gas content in bubbles, m_b, as follows

$$\frac{dc_b(t)}{dt} = \frac{16\pi f_n D_g r_g c_g(t)c_g(t)}{m_b(t)} - \frac{b}{2}c_b(t) \tag{32}$$

$$\frac{dn_b}{dt} = 4\pi r_b(t) D_g c_g(t) - \frac{b}{2} m_b(t) \tag{33}$$

In Eq. (33) f_n is the bubble nucleation factor, and c_g and r_g are the gas atom concentration and radius, respectively. In general, the value of f_n is less than one reflecting the premise that gas-bubble nucleation within the fuel matrix requires the presence of vacancies/vacancy clusters in order to become viable. The value of f_n is estimated based on the hypothesis that gas-atom diffusion occurs by a vacancy mechanism and that a 2 gas atom cluster is a stable nucleus. In this case f_n is approximately the bulk vacancy concentration (i.e., $\approx 10^{-4}$).

The 1st term on the right hand side (rhs) of Eq. (33) can be interpreted to represent the generation rate of "average" size bubbles of radius r_b. For every 2 atom bubble that is nucleated, $2/m_b$ of a bubble of radius r_b appears. In other words, nucleation of m_b two-atom clusters leads to the gain of one bubble of radius r_b. This "average size" bubble is in the peak region of the bubble-size distribution.

Both "whole" bubble destruction and gas-atom "chipping" from bubbles are included (last terms on right-hand side) in Eq. (32) and (33) in order to capture the behaviour of an average size bubble (that characterizes the full bubble-size distribution). Within the full bubble-size distribution there are bubbles that are destroyed by one fission fragment collision (e.g. bubbles smaller than a critical size) and others that are only partially damaged (e.g. bubbles larger than a critical size). Including b in both Eq. (32) and (33) is an attempt to depict these processes using a simplified formulation that enables an analytical solution for swelling. If $bc_b/2$ was not included in Eq. (32), then the density of bubbles could never decrease due to irradiation. Likewise if $bm_b/2$ was not included in Eq. (33), the number of atoms in a bubble could never decrease. However, the equal partition of gas-atom re-solution between these two mechanisms, as implied from the use of same re-solution parameter b in Eqs. (32) and (33) is an assumption that remains to be tested experimentally.

Due to the strong effect of irradiation-induced gas-atom re-solution, in the absence of geometric contact, the bubbles stay in the nanometer size range. The density of bubbles increases rapidly early in the irradiation. Subsequently, at longer times, the increase in bubble concentration occurs at a much-reduced rate. Based on the above considerations, the left-hand side of Eq. (32) is set equal to zero. This approximation will be more reasonable for larger values of t. A solution for c_b in terms of m_b and c_g is then given by

$$c_b = \frac{16\pi f_n r_g D_0 c_g^2}{b_0 m_b(t)} \tag{34}$$

46

The quantities c_g, c_b and m_b in Eqs (31-34) represent average values. For example, $c_b(t)$ bubbles each containing $m_b(t)$ gas atoms represents the average value of the bubble size distribution at time t. In general, r_b is related to m_b through the gas law and the capillarity relation. Using a modified Van der Waals gas law,

$$\frac{2\gamma}{r_b}\left(\frac{4}{3}\pi r_b^3 - h_s b_v m_b\right) = m_b kT \qquad (35)$$

where γ is the surface tension, b_v is the van der Waals constant for Xe, k is Boltzmann's constant, T is the absolute temperature, and h_s is a fitting parameter that for a given T makes Eq. (35) equivalent to the hard-sphere equation of state [10].

For bubbles in the nanometer size range an approximate solution to Eq. (35) is given by

$$r_b(t) = \left(\frac{3h_s b_v m_b(t)}{4\pi}\right)^{1/3} \qquad (36)$$

Using Eq. (36) and an argument similar to that used to derive Eq. (34), the steady-state solution to Eq. (33) is given by

$$m_b(t) = \left(\frac{3h_s b_v}{4\pi}\right)^{1/2}\left(\frac{4\pi D_0 c_g(t)}{b_0}\right)^{3/2} \qquad (37)$$

According to Speight [11], the fraction of gas f_s that diffuses to the grain boundary of grains of diameter d_g can be approximated by

$$f_s = \frac{8}{d_g}(D_g t)^{1/2} - \frac{6}{d_g^2}D_g t \qquad (38)$$

Imposing gas-atom conservation, i.e., requiring that the sum of the gas in solution, in intragranular bubbles, and on the grain boundary is equal to the amount of gas generated, the term $c_g(t)$ is determined as

$$c_g(t) = \frac{-(1+f_s)+\left[(1+f_s)^2 + 64\pi f_n r_g D_g \dot{f} \beta t/b\right]^{1/2}}{32\pi f_n r_g D_g /b} \qquad (39)$$

where β is the number of gas atoms produced per fission event.

Following the work of Wood and Kear [12], grain boundary bubble nuclei of radius R_b are produced until such time that a gas atom is more likely to be captured by an existing nucleus than

to meet another gas atom and form a new nucleus. An approximate result for the grain-boundary bubble concentration is given by

$$C_b = \left(\frac{8zaK}{12^{1/3} \pi^2 \xi D_g \delta} \right)^{1/2}$$

(40)

where a is the lattice constant, z is the number of sites explored per gas-atom jump, δ is the width of the boundary, ξ is a grain-boundary diffusion enhancement factor, and K is the flux of gas-atoms per unit area of grain boundary.

The intergranular bubble nucleation and growth formulation incorporated here is based on the assumption that, although the effect of radiation-induced re-solution on intergranular bubble behavior is not negligible, a reasonable approximation can be obtained by neglecting such effect in the governing equations [13].

Under the above considerations, the flux K of atoms at the grain boundary is given by

$$K = \frac{d_g}{3} \frac{dc_g}{dt} \frac{d(f_s t)}{dt}$$

(41)

Differentiating Eq. (39)

$$\frac{dc_g}{dt} = \frac{\beta \dot{f} - c_g df_s / dt}{\left(1 + f_s + 32\pi f_n r_g D_g c_g / b \right)}$$

(42)

where, using Eq. (38)

$$\frac{d(f_s t)}{dt} = \frac{12}{d_g} \left(\sqrt{\frac{D_g t}{\pi}} - \frac{D_g t}{d_g} \right)$$

(43)

The concentration of gas on the grain boundaries, C_g is given by

$$C_g(t) = \frac{d_g}{3} f_s(t) c_g(t)$$

(44)

and the average number of gas atoms in a grain boundary bubble is

$$N_b(t) = \frac{C_g(t)}{C_b(t)}$$

(45)

The radius of a grain boundary bubble is obtained from the solution to Eq. (35), i.e.

$$R_b = \left[\frac{3h_s b_v m_b}{8\pi} + \sqrt{\left(\frac{3h_s b_v m_b}{8\pi}\right)^2 - \left(\frac{m_b kT}{8\pi\gamma}\right)^3} \right]^{1/3}$$

$$+ \left[\frac{3h_s b_v m_b}{8\pi} - \sqrt{\left(\frac{3h_s b_v m_b}{8\pi}\right)^2 - \left(\frac{m_b kT}{8\pi\gamma}\right)^3} \right]^{1/3}$$

(46)

The fractional swelling due to fission gas is thus given by

$$\left(\frac{\Delta V}{V}\right)_g = \frac{c_g a^3}{4} + \frac{4\pi}{3}\left(r_b^3 c_b + R_b^2 C_b \frac{6}{d_g}\right)$$

(47)

where the first term at the right-hand-side of Eq. (47) accounts for the contribution of the gas in dynamic solution, and the second term for the contributions of both intragranular and intergranular bubbles, respectively.

Finally, the fraction of gas in dynamic solution (i.e. not in bubbles) is given by

$$X(t) = \frac{c_g(t)}{c_g(t) + C_g(t) + n_b(t)c_b(t)}$$

(48)

In general, in an irradiation environment where bubble nucleation, gas-atom diffusion to bubbles, and irradiation-induced re-solution are operative, a differential growth rate between bubbles of different size results in a peaked mono-modal size distribution [14]. The position of the peak in the bubble-size distribution that occurs under these conditions is defined by the balance between diffusion of gas-atoms to bubbles and irradiation-induced re-solution of atoms from bubbles. As more gas is added to the lattice (e.g., due to continued fission), the gas-atom diffusion flux to bubbles increases and the peak shifts to larger bubble sizes and decreases in amplitude, resulting in an increased level of bubble swelling with increased burn-up. The model presented in this section describes the average behavior of this peak as a function of burn-up.

4.2 Calculation of bubble-size distribution on grain boundaries

Let $n(r)dr$ be the number of bubbles per unit volume on the grain boundaries with radii in the range r to $r + dr$. Growth by gas atom collection from fission gas diffusing from the grain interior removes bubbles from this size range, but these are replaced by the simultaneous growth of smaller bubbles. The distribution of intragranular gas consists of a substantial concentration of fission-gas atoms in solution due to the strong effect of irradiation-induced gas-atom re-solution. Bubbles appear on the grain boundaries due to the reduced effect of re-solution ascribed to the strong sink-like property of the boundary, enhanced gas-atom diffusion on the

boundary, and a sizeable reduction in the bubble nucleation rate as compared to that occurring in the grain interior. A differential growth rate between bubbles of different size leads to a net rate of increase in the concentration of bubbles in the size range r to $r + dr$. This behavior is expressed by

$$\left[\frac{dn(r)}{dt}\right]dr = -\frac{d}{dr}\left[n(r)\frac{dr}{dt}\right]dr .$$ (49)

The growth rate (dr/dt) of a particular bubble is related to the rate (dm/dt) at which it absorbs gas from the matrix. The rate of precipitation is controlled by the grain-boundary gas-atom diffusion coefficient ξD_g and the average concentration C_g of fission gas retained by the boundary.

Studies on the evolution of helium bubbles in aluminum during heavy-ion irradiation at room temperature have shown that bubble coarsening can take place by radiation-induced coalescence without bubble motion [15]. This coalescence (called sputtering coalescence) is the result of the net displacement of Al atoms out of the volume between bubbles initially in close proximity. The resulting non equilibrium-shaped bubble evolves toward a more energetically favorable spherical shape whose final size is determined by the equilibrium bubble pressure.

In what follows it is assumed that the observed intergranular bubble coalescence events occur primarily by the sputtering coalescence mechanism. This mechanism should also be operative for intragranular bubbles, but will have a limited effect due to the small size of the bubbles compared to the inter-bubble spacing.

Bubble coalescence without bubble motion can be understood on the basis of a difference in the probability for an atom to be knocked out of the volume between a pair of bubbles and the probability of an atom to be injected into this inter-bubble volume. If the bubbles contained the same atoms as that comprising the inter-bubble volume, the net flux of atoms out of the inter-bubble volume would be zero. However, since the gas bubbles contain fission gas and not matrix atoms, the flux of atoms into the inter-bubble volume is reduced by the bubble volume fraction, i.e., the net flux out of volume is proportional to $\lambda V - \lambda(V - V_B)$, where λ is the atom knock-on distance, and V_B is the intergranular bubble volume fraction. It is assumed that most of the impacted atoms receive enough energy to travel distances λ on the order of the inter-bubble spacing. Thus, assuming that the atom displacement rate is proportional to the fission rate, the net rate of change in the concentration of bubbles in the size range r to $r + dr$ due to bubble coarsening without bubble motion is given by

$$\left[\frac{dn(r)}{dt}\right]dr = \frac{6}{d_g}\lambda\delta_s \dot{f} \pi r^2 n(r)dr ,$$ (50)

where the effective grain-face-bubble volume is assumed to be disk-shaped (lenticular) with volume = $\delta_s\pi r^2$, and where δ_s is the thickness of the material undergoing sputtering. For a lenticular bubble with radius of curvature ρ the equivalent radius of a spherical bubble is given by

$$r = \rho f(\theta)^{1/3}$$ (51)

where

50

$$f(\theta) = 1 - \frac{3}{2}\cos(\theta) + \frac{1}{2}\cos^2(\theta) \tag{52}$$

and

$$\cos(\theta) = \frac{\gamma_{gb}}{2\gamma}, \tag{53}$$

where γ_{gb} is the grain boundary energy. In Eq. (50), it is assumed that bubble coalescence is approached by the gradual erosion of material between the bubbles. Thus, Eq. (50) expresses a differential shrinkage rate between bubbles of different size due to the agglomeration of smaller bubbles by larger bubbles that leads to a net rate decrease in the concentration of bubbles in the size range r to $r + dr$

The overall net rate of change of the concentration of bubbles in a given size range is derived by subtracting the right-hand side of Eq. (50) from that of Eq. (49):

$$\frac{dn(r)}{dt}dr = -\frac{d}{dr}\left[n(r)\frac{dr}{dt}\right]dr - \frac{6}{d_g}\lambda\delta_s\,\dot{f}\,\pi r^2 n(r)dr. \tag{54}$$

The equilibrium population of bubbles is obtained by setting Eq. (51) to zero

$$-n(r)\frac{d}{dr}\left[\frac{dr}{dt}\right] - \frac{dr}{dt}\frac{dn(r)}{dr} - \frac{6}{d_g}\lambda\delta_s\,\dot{f}\,\pi r^2 n(r)dr = 0. \tag{55}$$

Equation (55) must be solved subject to the relevant boundary condition. In general, this boundary condition concerns the rate at which bubbles are formed at their nucleation size r_0. The rate of bubble nucleation is provided by the Wood-Kear nucleation mechanism [12] where on the grain boundary the average time τ_b for a gas atom to diffuse to an existing bubble (as discussed above this is the time at which bubble nucleation would essentially cease) is given by

$$\tau_b = \frac{1}{\pi\xi D_g C_b}. \tag{56}$$

Thus, from Eq. (56) it follows that the bubble nucleation rate is given by

$$\frac{dC_b}{dt} = \eta\frac{C_b}{\tau_b}. \tag{57}$$

where η is a proportionality constant that is determined by imposing the conservation of gas atoms.

From a consideration of the growth rate of freshly nucleated bubbles it follows that

$$n(r_0)dr = \frac{3\eta}{d_g}\left(\frac{C_b}{\tau_b}dr\right)\Big/(dr/dt)_{r=r_0}. \tag{58}$$

The observed grain boundary bubbles are a combination of spherical lenticular shaped objects whose size is substantially larger than the estimated thickness of the grain boundary (see Table 3). In general, the solubility of gas on the grain boundary is substantially higher than in the bulk material. The gas concentration on the boundary will increase until the solubility limit is reached (approximately given by τ_b), whereupon the gas will precipitate into bubbles. Thus, the rate at which a grain boundary bubble adsorbs gas is approximately given by

$$\left(dm/dt\right)_{r=r_0} = b_v C_g /\left(4\tau_b \pi r_0^3 /3\right), \tag{59}$$

where C_g is given by Eq.(44). Using Eq. (35)

$$\frac{dm}{dt} == \frac{16\pi\gamma\left(kTr^3 + 3\gamma b_v r^2\right)}{3\left(rkT + 2\gamma b_v\right)^2} \frac{dr}{dt} \tag{60}$$

Combining Eqs. (59) and (60)

$$\left(dr/dt\right)_{r=r_0} = \frac{3C_g b_v \left(rkT + 2\gamma b_v\right)^2}{16\pi\gamma\left(4\tau_b \pi r_0^3 /3\right)\left(kTr^3 + 3\gamma b_v r^2\right)} \tag{61}$$

Subsequent to intergranular bubble nucleation, gas solubility on the boundary will drop to a relatively low value and gas arriving at the boundary will be adsorbed by the existing bubble population. The rate at which a grain boundary bubble adsorbs gas is approximately given by

$$dm/dt = 12\pi r \xi D_g C_g /d_g. \tag{62}$$

Combining Eq. (60) and (62)

$$dr/dt = \frac{9r\xi D_g C_g \left(rkT + 2\gamma b_v\right)^2}{4\gamma d_g \left(kTr^3 + 3\gamma b_v r^2\right)} \approx \frac{3b_v \xi D_g C_g}{d_g r}. \tag{63}$$

Using the approximation on the right-hand side of Eq. (63), Eq. (55) becomes

$$n(r)\frac{3b_v \xi D_g C_g}{d_g r^2} - \frac{3b_v \xi D_g C_g}{d_g r}\frac{dn(r)}{dr} - \frac{6}{d_g}\lambda\delta_s \dot{f} \pi r^2 n(r) = 0, \tag{64}$$

The solution of Eq. (64) subject to the boundary condition expressed by Eq. (58) and (61) is

$$n(r) = \frac{64\eta\gamma C_b^2 \pi^2 r^3 \left(kTr^3 + 3\gamma b_v r^2\right)\exp\left[-\kappa\left(r^4 - r_0^4\right)\right]}{3b_v C_g d_g \left(rkT + 2\gamma b_v\right)^2}, \tag{65}$$

where

$$\kappa = \frac{\pi \dot{f} \lambda\delta_s}{2b_v \xi D_g C_g}. \tag{66}$$

4.3 Comparison of calculated intergranular bubble-size distribution with the measured data

The values of the key parameters used in the model are given in Table 9. Many of them are known from the literature [16]; the values of the others (e.g. ξ and D_g) resulted from the fitting of the present theory with measured data of bubble populations. The value used for D_g is consistent with that used in the homogenization analysis in Section 2 [5]. The intergranular bubble size depends on the value of ξ (see Eq. (40) and Table 9), which is a grain-boundary gas-atom diffusion enhancement factor that reflects the fact that grain boundary diffusion is decidedly faster than grain lattice diffusion [17,18]. The effect of ξ on the intergranular bubble nucleation is visible in Eq. (40). By increasing ξ the intergranular bubble density is reduced with a commensurate increase in bubble size. The larger value used for ξ for the non-annealed miniplates reflects the increase in diffusivity with decreased molybdenum content.

Table 9. Values of parameters used in the calculations

Parameter	Value	Reference
β	0.25	Olander [16]
ξ	7×10^3 4×10^4	(annealed) [17] (non-annealed) This work
$b_0\,(b = b_0\,\dot{f}\,)$	$1 \times 10^{-24}\ \mathrm{m^3}$	This work
$D_0\,(D_g = D_0\,\dot{f}\,)$	$2.5 \times 10^{-41}\ \mathrm{m^5}$	This work
r_g	0.216 nm	Olander [16]
γ	$0.8\ \mathrm{J\,m^{-2}}$	This work
$\cos(\theta)$	0.2	[19]
b_v	$8.5 \times 10^{-23}\ \mathrm{m^3/atom}$	Olander [16]
f_n	5×10^{-3}	Spino/Rest [10]
h_s	0.6	Spino/Rest [10]
$\delta_s = \delta$	$1 \times 10^{-9}\ \mathrm{m}$	[17,18]
λ	$2 \times 10^{-7}\ \mathrm{m}$	Olander [16]

The calculated distribution was obtained by integrating Eq. (65) over the experimentally defined bin sizes Δ_i, i.e. the bubble density $N(\Delta_i)$ in units of $\mathrm{m^{-2}}$ is

$$N(\Delta_i) = \frac{d_g}{3} \int_{\Delta_0 + (i-1)\Delta}^{\Delta_0 + i\Delta} n(r)\,dr \qquad (67)$$

where Δ_0 is the minimum bubble size observed.

Table 10 shows a description of fuel used in the analysis. This data base consists of both as-atomized and γ-annealed specimens. From table 10, the range of burn up is from $30 - 49$ at% U-235, fission rate from $2.3 - 7 \times 10^{14}\ \mathrm{f/cm^3}$-s, temperature from $66 - 185\ ^\circ\mathrm{C}$, and Mo content from $6 - 10$ wt.%. As shown in Table 11, the values for the critical parameters D_g and b listed in Table 9 were estimated by comparing the calculated intragranular average bubble size and density to measured results [6]. The value for D_g is comparable to the one used by Bleiberg [5] for irradiation induced mixsing. The remaining critical parameter ξ was determined by best overall interpretation of the measured intergranular bubble-size distributions for the γ-annealed

and for the as-atomized specimens, respectively. The calculated results shown in Table 11 can be brought more in line with the data by decreasing D_g, increasing b, or both. This then would require a commensurate decrease in ξ. For this exercise to be meaningful measured intragranular bubble-size distributions are required.

Table 10. Description of fuel used in the analysis

Test	Plate AG ID	Plate ID	Fuel property	Burnup, at% U-235	Fission rate (10^{14}) f/cm^3-s	Time (days)	Fuel Temp (^{o}C)
RERTR-3	580H	Z03	U-10Mo(a,γ)	32	5.3	48	121
RERTR-3	580C	Y01	U-10Mo(m,γ)	30	4.8	48	109
RERTR-1	-	V002	U-10Mo(a)	39	3.8	94	66
RERTR-3	580G	V07	U-10Mo(a)	30	5.1	48	122
RERTR-3	580W	V03	U-10Mo(a)	38	6.3	48	149
RERTR-3	580Z	S03	U-6Mo(a)	39	7.0	48	158
RERTR-5	600AG	R6007F	U-7Mo(a)	37	2.4	116	185
RERTR-5	600M	V6019G	U-10Mo(a)	49	2.9	116	142
RERTR-5	600AH	V8005B	U-10Mo(a)	37	2.4	116	170

a: atomized, γ: annealed at 800 ^{o}C for 70-100 hours before plate fabrication, m: machined

Table 11. Intragranular results using estimated values for D_g and b

	Calculated	Data [4]
Bubble diameter (nm).	2.1	≈ 2
Bubble density (cm^{-3})	1.4 x 10^{18}	≈ 3 x 10^{18}
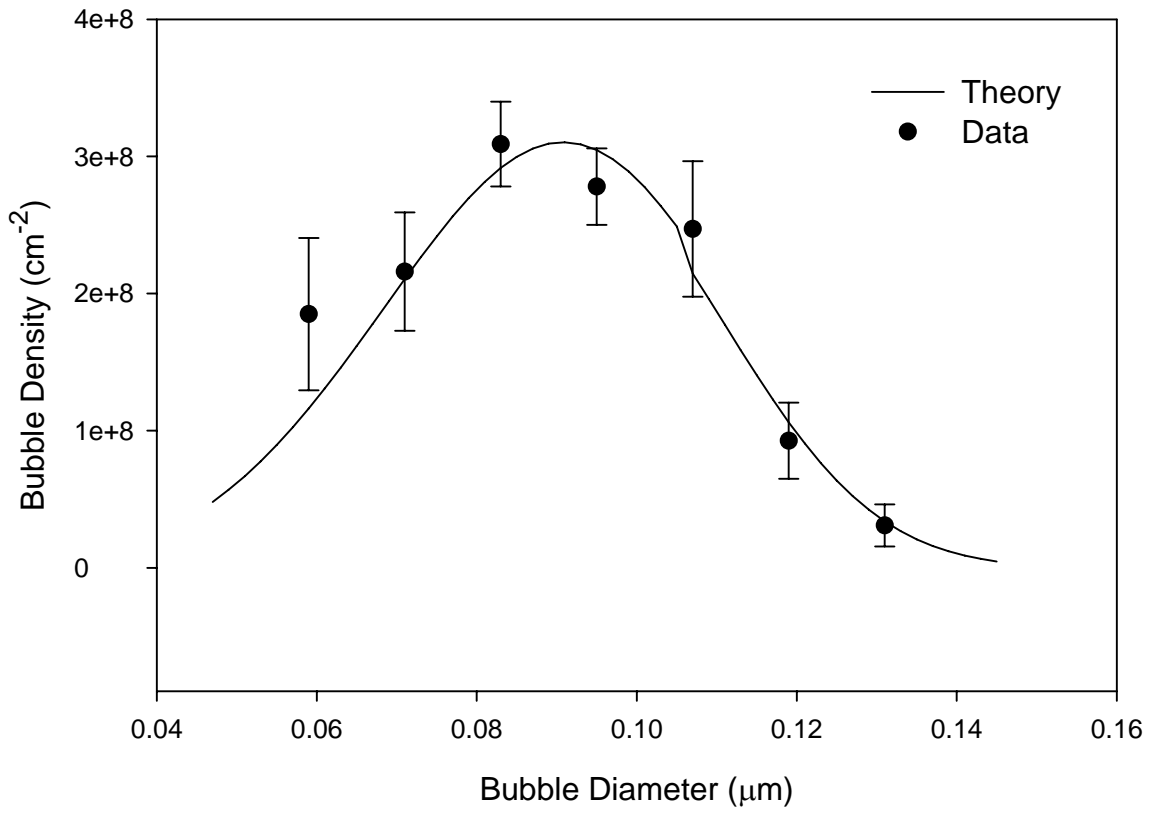
Fig. 39 Calculated and measured intergranular bubble-size distribution for Z03 plate. Atomized and γ-annealed U-10Mo.

Fig. 40 Calculated and measured intergranular bubble-size distribution for Y01 plate. Machined and γ-annealed U-10Mo.

Fig. 41 Calculated and measured intergranular bubble-size distribution for V03.
As-atomized U-10Mo.

Grain-boundary bubble size distribution for V07
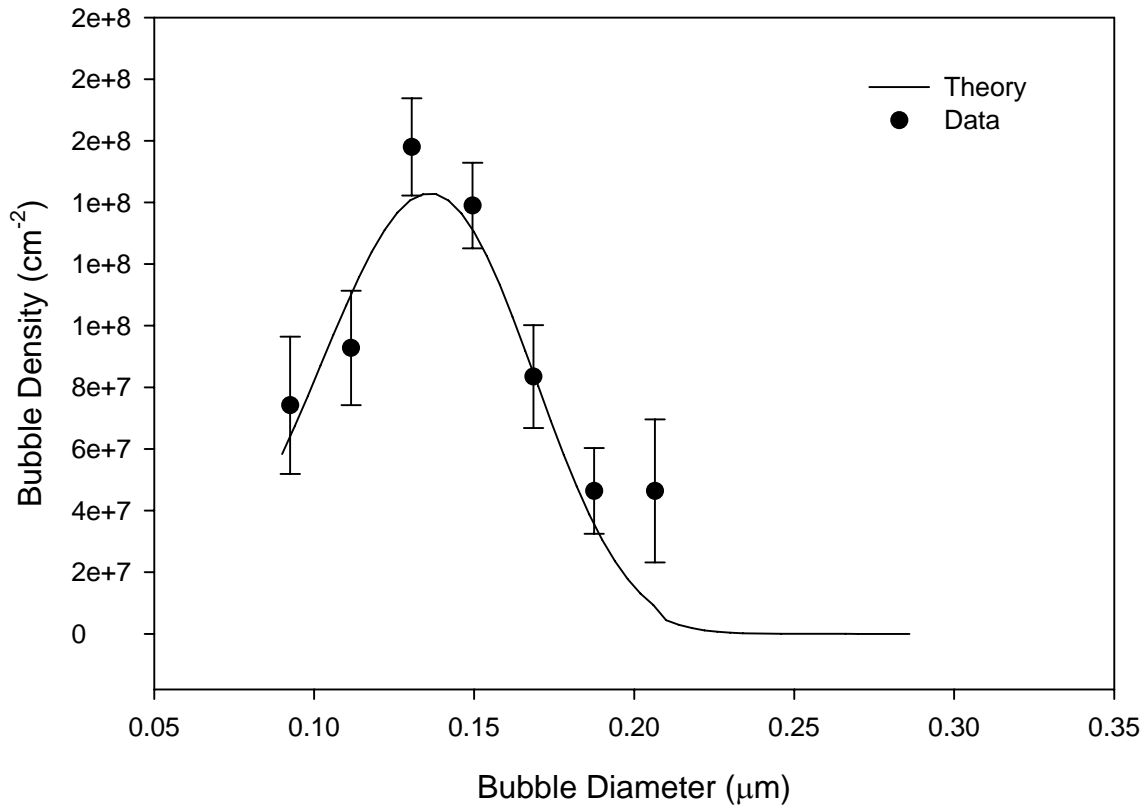
Fig. 42 Calculated and measured intergranular bubble-size distribution for V07.
As-atomized U-10Mo.

Grain-boundary bubble size distribution for V8005B
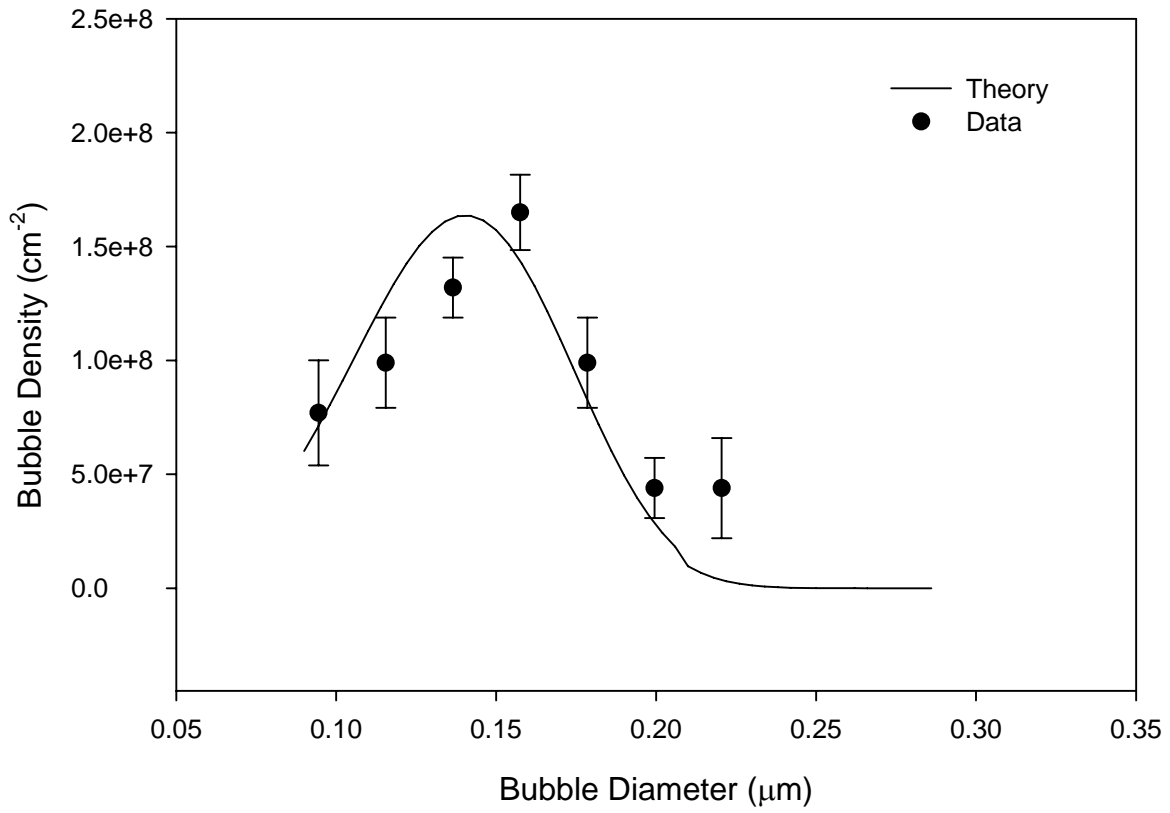
Fig. 43 Calculated and measured intergranular bubble-size distribution for V8005B. As-atomized U-10Mo.

Fig. 44 Calculated and measured intergranular bubble-size distribution for
V6019G. As-atomized U-10Mo.
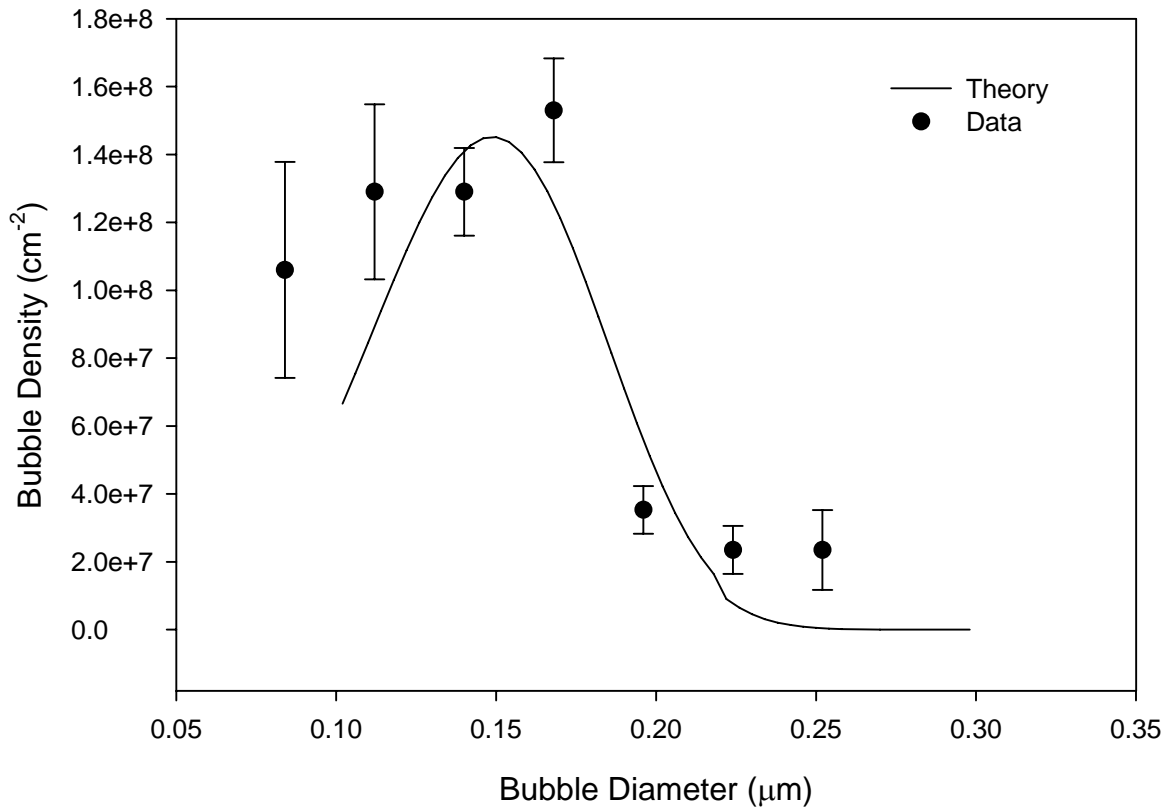
Fig. 45 Calculated and measured intergranular bubble-size distribution for V002.
As-atomized U-10Mo.

Fig. 46 Calculated and measured intergranular bubble-size distribution for S03.
As-atomized U-6Mo.

Grain-boundary bubble size distribution for R6007F
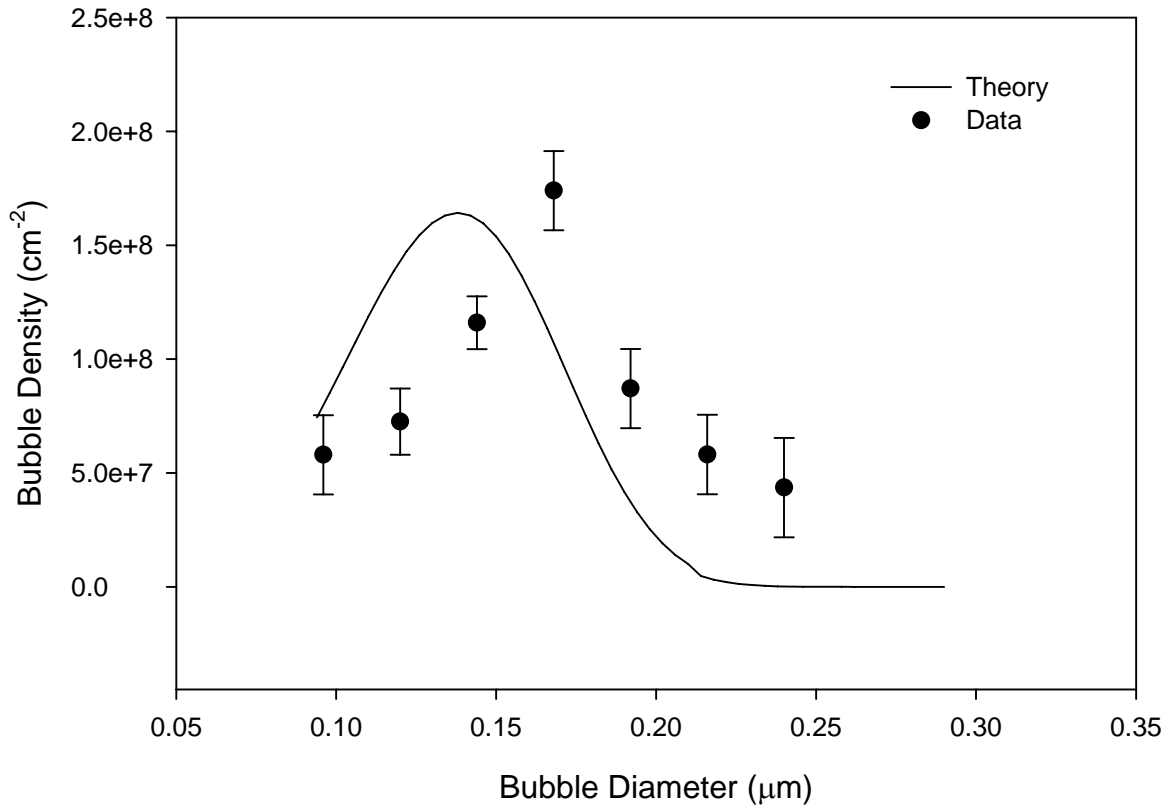
Fig. 47 Calculated and measured intergranular bubble-size distribution for R6007F. As-atomized U-7Mo.

Figures 39 and 40 show the calculated and measured intergranular bubble-size distribution for γ-annealed plates. Figure 39 is atomized whereas Fig. 40 is machined. Figures 41 - 47 show calculated and measured intergranular bubble-size distribution for as-atomized plates. Figures 41-45 are for 10 wt% Mo whereas Figs. 46 and 47 are for 6 and 7 wt% Mo, respectively. As is evident from Figs. 39 - 47, in general, the model calculations are in remarkable agreement with the data. The error bars are shown on the measured data reflect the measurement uncertainties discussed in Subsection. 3.1. The larger deviation between calculated and measured results shown for the plates in Figs 46 and 47 is most likely due to the lower as fabricated Mo content and, thus, requires different values for D_g and ξ.

4.4 Calculation of intragranular bubble-size distribution: effect of uncertainties in materials properties

Intragranular bubbles are subject to destruction by irradiation-induced re-solution. In general, the average intragranular bubble in UMo is small enough that whole bubble destruction is a reasonable assumption. In this case, the net rate of change in the concentration of bubbles in the size range r to $r + dr$ due to destruction by fission fragments is given by

$$\left[\frac{dn(r)}{dt}\right]dr = 2\lambda_f \dot{f} \pi r^2 n(r)dr \tag{68}$$

where λ_f is the average range of a fission fragment. Replacing the last term in Eq. (54) with Eq. (68) and using the boundary condition

$$n(r_0)dr = \left(\frac{c_b}{\tau_b}dr\right)/(dr/dt)_{r=r_0} \tag{69}$$

where

$$\tau_b = \frac{1}{\pi D_g c_b} \tag{70}$$

and

$$\frac{dr}{dt} = \frac{b_v D_g c_g}{r} \tag{71}$$

one obtains

$$n(r) = \frac{\pi c_b^2 r \exp\left[-\kappa\left(r^4 - r_0^4\right)\right]}{b_v c_g} \tag{72}$$

where

$$\kappa = \frac{\pi \dot{f} \lambda}{2 b_v D_g c_g} \tag{73}$$

In order to proceed λ_f needs to be expressed in terms of the re-solution rate b. Whole bubble destruction is included in Eq. (31) through via the last term in Eq. (32), i.e.

$$\frac{dc_b(t)}{dt} \approx -\frac{b}{2}c_b(t).$$

(74)

Using Eq. (67), (68) and (72) in Eq. (74), after utilizing an approximation for the Error function, one obtains

$$\lambda_s = \frac{9b_0^2}{128b_v D_0 c_g},$$

(75)

Figure 48 shows calculated intragranular bubble size distributions for 3 values of the gas-atom diffusivity, and re-solution rate, respectively. The results shown in Fig. 48 indicate the sensitivity of the calculated distributions to variations in the values of these critical parameters. One of the major challenges in the field of fission gas behavior in nuclear fuels is the quantification of critical materials properties. There is a direct correlation between the accuracy of the values of critical properties and the confidence level that the proposed underlying physics is realistic.
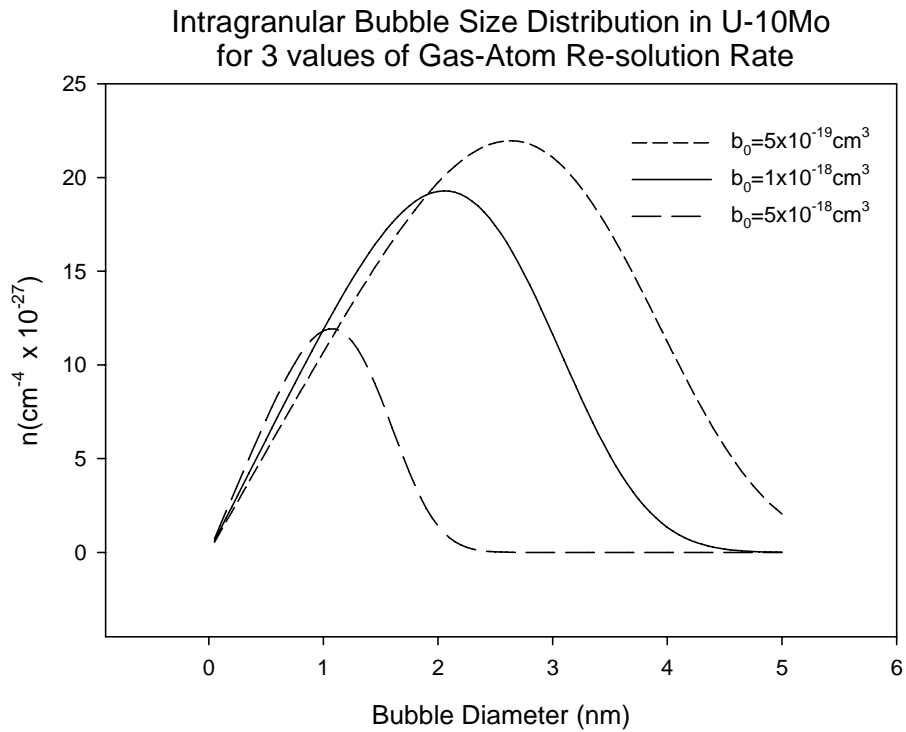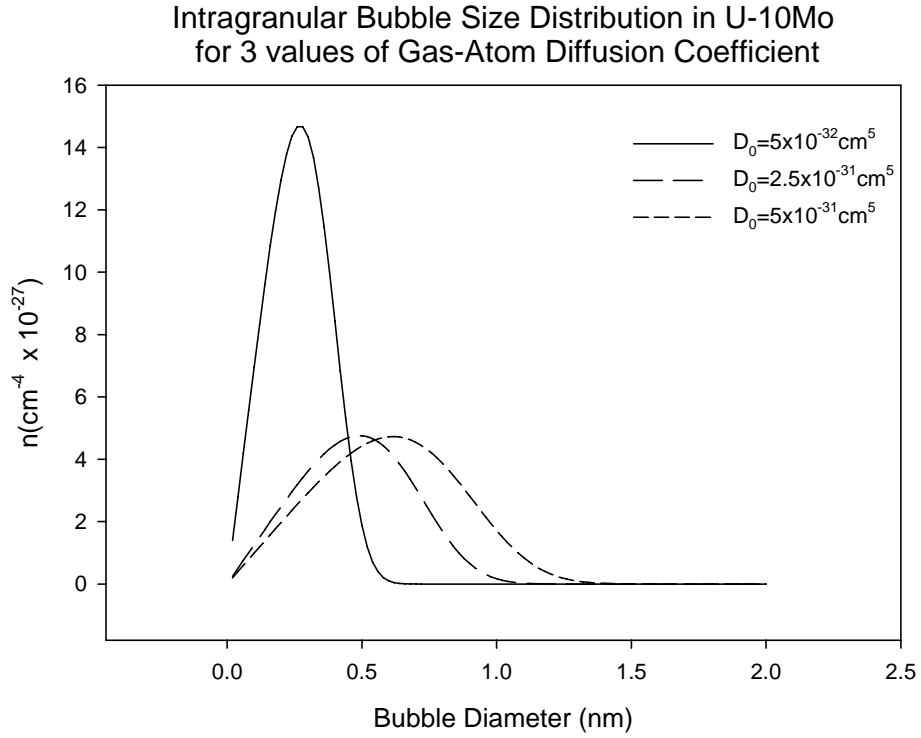
Fig. 48 Calculated intragranular bubble size distributions for 3 values of the gas-atom diffusivity ($D_g = D_0 \dot{f}$) and gas-atom re-solution rate ($b = b_0 \dot{f}$).

5. Conclusions

1. Analysis using a simple diffusion model shows that the grain boundaries are not completely homogenized by irradiation under typical RERTR test conditions.

2. Fission gas bubbles visible in SEM micrographs first appear on the grain boundaries in U-Mo alloy fuels from RERTR-1, 2, 3 and 5 tests.

3. The plates with γ-phase annealed powders have smaller bubbles and lower volume fractions than the plates with as-fabricated powders.

4. Although there are considerable errors, after an initial incubation period the average bubble size increases with fission density and shows saturation at high fission density.

5. The γ-annealed powder plates have a higher bubble density per unit grain boundary length than the as-atomized powder plates. The measured bubble number densities per unit grain boundary length for as-atomized powder plates are approximately constant with respect to burnup.

6. Bubble density per unit cross section area was calculated using the density per unit grain boundary length data. The grains were modeled as tetrakaidecahedrons. Direct measurements for some plates were also performed and compared with the calculated quantities. Bubble density per unit grain boundary surface area was also calculated by using the density per unit grain boundary length data. These data were used as input for mechanistic modeling.

7. The contribution to the total fuel swelling by fission gas bubbles is very small in the pre-recrystallization regime. This suggests that in the pre-transition regime a considerable concentration of fission gas remains in atomic solution or in small bubbles not resolvable by SEM.

8. Calculations of intergranular bubble size distribution made with a new mechanistic model of grain boundary bubble formation kinetics is consistent with the measured distributions.

9. The gas-atom diffusion enhancement factor for grain boundaries was determined for as-annealed powder plates to be $\approx 10^4$ in order to obtain agreement with the measured distributions. This value of enhancement factor is consistent with values obtained in the literature. The enhancement factor is six times higher for as-fabricated powder plates than for the annealed plates due to the lower Mo content on the boundaries.

10. Model predictions are sensitive to various model parameters such gas-atom diffusivity and re-solution rate. Improved predictive capability requires an accurate quantification of these critical materials properties and measurement data.

References

[1]   K.H. Kim et al., *J. Nucl. Mater*, 245 (1997) 179.
[2]   J.M. Park et al., *RERTR Conf.*, 2006. Available from: http://www.rertr.anl.gov/index.html
[3]   W. Sinkler et al., ANL Memo to M.K. Meyer, WS-2000.
[4]   M.L. Bleiberg et al., *J. Appl. Phys.*, 27(11) (1956) 1270.
[5]   M.L. Bleiberg, *J. Nucl. Mater.*, 2 (1959) 182.
[6]   S. Van Den Berghe at al., *RERTR conf.*, 2007. Available from:
        http://www.rertr.anl.gov/index.html
[7]   R.T. DeHoff and F.N. Rhines, *Quantitative microscopy*, McGraw-Hill, New York, 1968.
[8]   Yeon Soo Kim, G.L. Hofman, M.R. Finlay, J.L. Snelgrove, Milestone report on
        Postirradiation Examinations: RERTR-3, 4 and 5, ANL, September 2005.
[9]   Yeon Soo Kim et al., *RERTR conf*, 2007. Available from:
        http://www.rertr.anl.gov/index.html
[10]   J. Spino, J. Rest, W. Goll, C.T. Walker, *J. Nucl. Mater*, 346 (2005) 131.
[11]   ]M.V. Speight, *Nucl. Sci. Eng.* 37 (1969) 180.
[12]   M.H. Wood, K.L. Kear, *J. Nucl. Mater* 118 (1983) 320.
[13]   J. Rest, *J. Nucl. Mater*, 321 (2003) 305.
[14]   M.V. Speight, *J. Nucl. Mater*, 38 (1971) 236.
[15]   R.C. Birtcher, S.E. Donnelly, C. Templier, *Phys. Rev. B*, 50 (1994) 764.
[16]   D.R. Olander, Fundamental Aspects of Nuclear Reactor Fuel Elements, Technical
        Information Center, ERDA, USA, 1976.
[17]   N.A. Gjostein, in *Diffusion*, Chapter 9, American Society for Metals, Metals Park, Ohio
        (1973) 272.
[18]   J.C. Fisher, *J. Appl. Phys.*, 22 (1951) 74.
[19]   E.D. Hondros, in *Precipitation Processes in Solids*, K.C. Russell and H.I. Aaronson, Eds.,
        The Metallurgical Society of AIME (1976) 1.